PR12-16-009

Longitudinal and Transverse Target Correlation Asymmetries in Wide Angle Compton Scattering

A Proposal to Jefferson Lab PAC 44

Zhihong Ye
Argonne National Lab

D. Nikolenko, I. Rachek, Yu. Shestakov
Budker Institute, Novosibirsk, Russia

G.B. Franklin, B. Quinn
Carnegie Mellon University, Pittsburgh, PA 15213

T. Averett, C. Perdrisat
College of William and Mary, Williamsburg, VA 23185

B. Dongwi, E. Christy, J. Nazeer, N. Kalantarians, M. Kohl, A. Liyanage
Hampton University, Hampton, VA 23668

G. Ron
Hebrew University of Jerusalem, Israel

N. Kivel
Helmholtz-Institut Mainz, Germany

C. Muñoz Camacho
Institut de Physique Nucleaire d'Orsay, IN2P3, BP 1, 91406 Orsay, France

W. Boeglin, P. Markowitz
Florida International University, Miami, FL 33199

J. Dunne, D. Dutta, L. Fassi, K. Adhikaari,
H. Bhatt, D. Bhetuwal, L.Ye
Mississippi State University, Mississippi State, MS 39762

V. Punjabi
Norfolk State University, Norfolk, VA 23504

A. Ahmidouch, S. Danagoulian
North Carolina A&T State University, Greensboro, NC 27411

M. Amaryan, G. Dodge, C.E. Hyde, A. Radyushkin,
L. Weinstein
Old Dominion University

R. Gilman, R. Ransome
Rutgers, The State University of New Jersey, Piscataway, NJ 08854

E. Piasetzky
Tel Aviv University, Israel

Z.-E. Meziani
Temple University, Philadelphia, PA 19122

T. Horn,
The Catholic University of America, Washington DC, 20064

A. Camsonne, J. P. Chen, E. Chudakov, J. Gomez, D. Gaskell, O. Hansen,
D. W. Higinbotham, M. Jones, C. Keppel, D. Mack, R. Michaels, B. Sawatzky,
G. Smith, S. Wood
Thomas Jefferson National Accelerator Facility, Newport News, VA 23606

J. R. M. Annand, D. I. Glazier, D. G. Ireland,

University of Glasgow, Glasgow, Scotland

T. Badman, E. Long, K. Slifer, B. Yale, R. Zielinski
University of New Hampshire, Durham, NH 03824

G. Cates, D. Crabb, D. Day(spokesperson), N. Dien,
D. Keller(spokesperson, contact), R. Lindgren,
N. Liyanage, V. Nelyubin, M. Yurov
J. Zhang(spokesperson)
University of Virginia, Charlottesville, VA 22904

G. Miller
University of Washington, WA 98195

P. Kroll
University of Wuppertal, North Rhine-Westphalia, Germany

A. Asaturyan, A. Mkrtchyan, H. Mkrtchyan, A. Shahinyan, V. Tadevosyan,
H. Voskanyan, S. Zhamkochyan
Yerevan Physics Institute, Yerevan 0036, Armenia

The Neutral Particle Spectrometer collaboration
`https://wiki.jlab.org/cuawiki/index.php/Collaboration`

June 6, 2016

Contents

Abstract

We propose an experiment to measure the initial state helicity correlation asymmetries A_{LL} in Real Compton Scattering (RCS) by scattering longitudinally polarized photons from a longitudinally (A_{LL}) polarized proton target at two photon energies 4 GeV (s = 8 (GeV/c)^2) and 8 GeV (s = 15 (GeV/c)^2) for the same scattering angle of θ_γ^{cm}=90°. We also propose scattering longitudinally polarized photons from a longitudinally (A_{LL}) and transversely (A_{LS}) polarized proton target at photon energy of 8 GeV (s = 15 (GeV/c)^2) at θ_γ^{cm}=120°. This experiment could potentially run in the same block of polarized target experiment with E12-13-011, E12-14-006 and E12-15-005 to make use of the very similar target setup already in place.

Two JLab RCS experiments, E99-114 and E07-002, demonstrated the feasibility of the experimental technique. Our experiment uses an untagged pure photon beam and the UVA/JLAB polarized target. The pure photon beam adds considerable photon intensity and reduction of overhead required for polarized target maintenance. The scattered photon is detected in the future NPS. The coincident recoil proton is detected in the Hall C magnetic spectrometer HMS.

Calculations by G. A. Miller in a constituent quark model reproduced the lower $s = 6.9$ GeV^2 K_{LL} experimental result but revealed a large disagreement with the GPD prediction for A_{LL}. It is but one of the goals of our proposal to test this prediction which could force a modification of our understanding of the high-t photo-induced processes such as RCS, pion photoproduction, and deuteron photo–disintegration. A measure of $A_{LL}$and the conclusions that can be drawn from the results would give insight into understanding quark orbital angular momentum in the proton.

The higher $s = 7.8$ GeV^2 K_{LL} experimental result does not compare to any predictions. This surprising result seems to indicate that K_{LL}does not have significant variation over change in s or center of mass angle. We propose to study further the cause of this extraordinary result by staying strictly within the domain of kinematics applicable to the Handbag approach and studying the s and θ_γ^{cm}dependence for both longitudinal and transverse target observables.

We request 835 hours of 3 μA at 4.4 GeV and 8.8 GeV electron beam energies to measure the polarization observables A_{LL} and A_{LS} to a statistical accuracy better than 5%. This measurement will significantly increase the available experimental information needed to move the GPD approach forward on RCS, one of the most fundamental processes.

1 Introduction

Significant progress has been made over the last decade in our understanding of exclusive reactions in the hard scattering regime. This progress had been made possible (in part) by data from Jefferson Lab on elastic electron scattering and Compton scattering from the proton and by a significant and increasingly sophisticated theoretical effort to exploit the richness of exclusive reactions at moderate momentum transfers.

The observation of scaling in Deep Inelastic Scattering (DIS) at relatively low momentum transfers, successfully understood within the framework of pQCD, suggested that the same interpretation would be fruitful when applied to exclusive reactions: elastic electron scattering, photo- and electro-production of mesons, and Compton scattering. This prospect was further supported by the fact that constituent counting rules [1, 2], which naturally govern reactions that conform to the pQCD picture, could describe certain exclusive reactions.

There is little doubt that the pQCD mechanism dominates at high energies. What has been lacking is a general agreement as to how high the energy must be for pQCD to be completely applicable. The argument on this point is driven by more than a difference of (theoretical) opinion. The unavoidable fact is that cross sections calculated in a pQCD framework have invariably been low when compared to data, sometimes by an order of magnitude or more[3, 4].

Results of experiments at Jefferson Lab on the proton contradict the predictions of pQCD: the recoil polarization measurements of G_E^p E93-027, E04-108 and E99-007, and the Real Compton Scattering (RCS) experiment E99-114. The G_E^p measurements [5, 6, 7] found that the ratio of F_2 and F_1, scaled by Q^2 demands a revision of one of the precepts of pQCD, namely hadron helicity conservation. Results from the RCS measurements [8, 9] are that the longitudinal polarization transfer K_{LL} is large and positive, contrary to the pQCD predictions for K_{LL}. These experiments provide a compelling argument that pQCD should not be applied to exclusive processes at energy scales of 5-10 GeV.

Fortunately, an alternate theoretical framework exists for the interpretation of exclusive scattering at intermediate energies [10, 11, 12, 15]. This alternative approach asserts the dominance of the handbag diagram in which the reaction amplitude factorizes into a subprocess involving a hard interaction with a *single quark*. The coupling of the struck quark to the spectator system is described by the Generalized Parton Distributions (GPD's) [16, 17]. Since the GPD's are independent of the particular hard scattering reaction, the formalism leads to a unified description of hard exclusive reactions. Moreover, the relationship between GPD's and the normal parton distribution functions provides a natural framework for relating inclusive and exclusive reactions.

The RCS experiment E99-114 produced an especially remarkable result; not only was the measurement of K_{LL} inconsistent with pQCD, it was found that the longitudinal polarization is nearly as large as that expected for scattering from a free quark.

The QCD factorization approach formulated in the framework of Soft Collinear Effective

Theory (SCET) can be used to develop a description of the soft-spectator scattering contribution [19, 21]. Recently a derivation of the complete factorization for the leading power contribution in wide angle Compton scattering has been worked out in the soft collinear effective theory. As factorization evolves and becomes less dependent on the assumption of restricted parton virtualities and parton transverse momenta RCS should receive the same level of attention that DVCS has. RCS have a complementary nature to DVCS in so far as in DVCS the GPDs are probed at small t while for RCS (and nucleon form factors) the GPDs are probed at large t.

The initial state helicity correlation can be used to probe a theoretical model in detail. According to the handbag approach their angle dependence is close to that of the subprocess $\gamma q \to \gamma q$ diluted by form factors which take into account that the proton is a bound state of quarks and which represent $1/x$ moments of GPDs. The electromagnetic nucleon form factors have been revised using the generalized parton distributions analysis by M. Diehl and P. Kroll [24]. The various theoretical efforts made to apply the handbag approach to wide angle compton scattering (WACS) have produced predictions for its polarization observables including $K_{_{LL}}$ and $A_{_{LL}}$ [12, 25]. In addition, a calculation of Miller [25] suggests that a measurement of $A_{_{LL}}$ in WACS would be a test of perturbative chiral symmetry and of the mass of the quarks participating in the hard scattering. At present the polarized observables so far measured are at limited kinematics to test any hangbag approach, where it is best if $-u$ and $-t$ are greater than 2.5 GeV^2 as a minimum condition for calculations to be applicable.

The polarized observables are essential for moving the framework forward. There was only one polarization measurement of $K_{_{LL}}$ made during E99-114, so a similar experiment (E07-002) [26] at higher s was undertaken in Hall C which acquire one more $K_{_{LL}}$ point [9]. An approved proposal PR12-14-006 to measure $A_{_{LL}}$requested beam time to measure kinematic points $P_1 : s, -t, -u = 8, -1.7, -4.5$ GeV^2, $P_2 : s, -t, -u = 8, -3.3, -2.9$ GeV^2 and $P_3 : s, -t, -u = 8, -5.4, -0.8$ GeV^2. Unfortunately the most relevant point, P_2, to study the theories using the handbag approach was not approved. Given the interesting experimental results for K_{LL} it is increasingly necessary to take measurements using kinematics for $-u$ and $-t$ that are greater than 2.5 GeV^2. The next step is to obtain additional measurements to try to create a suite of observables to explore the applicable kinematic landscape to provide as much information on the WACS phenomenology as possible.

The previous polarized observables measured so far are $K_{_{LL}}$and K_{LS}, the helicity of the incoming photon and the sideways polarization of the outgoing proton. The K_{LS} measurements [8, 9] agree with both the leading-quark and the pQCD approaches [30, 12, 25, 19, 20]. However, the results for $K_{_{LL}}$are completely unexpected. The $K_{_{LL}}$measurement [9] for $s, -t, -u = 7.8, 2.1, 4.0$ GeV^2 is in agreement with what was found in the previous JLab experiment [8] for $s, -t, -u = 6.9, 4.0, 1.1$ GeV^2. It is quite surprising to find consistent values for these different kinematics. For all theoretical predictions there are distinct variations over angle for the two-spin initial state helicity (L-type) correlations, seen in Fig. 1. This remarkable disagreement with predictions may be an indication that the measured kinematics

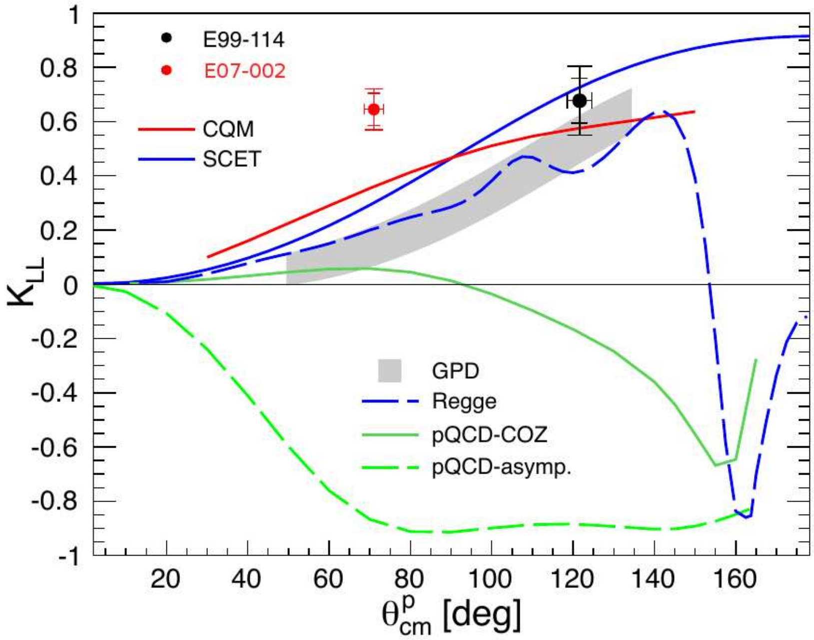

Figure 1: The new experimental result for K_{LL}. Also shown are the E99-114 value [52] and the calculations in different approaches: the pQCD [30] with the asymptotic and COZ distribution amplitudes [45], the extended Regge model [15], the GPD [12], shown as a gray band of uncertainty due to finite mass corrections [34], the CQM [46], and the SCET [18], figure taken from [9].

are still far from the asymptotic regime for the WACS process. This deviation from theory could be due to many possible neglected contributions. One possibility is the noncollinear effects in exclusive reactions and parton correlations in the nucleon. The K_{LL} increase may be related to significant roles observed in elastic electron-nucleon scattering of both quark orbital angular momentum and a $u-d$ diquark correlation [54, 55]. In any event, it is clear that more measurements are needed to understand this phenomenon. In this proposal, we are interested in exploiting the longitudinal and transversely polarized target to add to the kinematics and observables. We therefore propose a measurement of the polarization observable A_{LL} in Compton scattering at photon energy of 4.4 GeV ($s = 8$ GeV^2) and 8.8 GeV ($s = 15$GeV^2) at 90° center of mass angle and A_{LL} and A_{LS} at 8.8 GeV ($s = 15$GeV^2) at 120°.

The proposal is organized as follows. In Section 2 we describe in more detail the handbag formalism and the predictions for RCS, some results from experiments, and a summary of the physics goals of the proposed experiment. In Section 3 we describe the experimental approach and both the standard and the specialized equipment. In subsequent sections, we present our proposed measurements (Sec. 4), our expected results and beam time request

(Sec. 5). Finally, the proposal is summarized in Section 8.

2 Physics Motivation

2.1 Overview

In view of the remarks in the Introduction, we consider several interesting questions that motivate us to explore further the measurement of polarization observables in RCS at JLab:

1. What is the nature of the quark which absorbs and emits photons in the RCS process in the wide angle regime? Is it a constituent or a current quark?

2. If the GPD approach is correct, is it indeed true that the RCS reaction proceeds through the interaction of photons with a single quark?

3. What are the constraints on the GPD integrals imposed from the proposed measurement of the A_{LL} and A_{LS} observables?

In order to present a framework for addressing these issues, we next briefly discuss WACS in the soft-collinear effective theory, the handbag mechanism in the GPD conceptualization, and the handbag mechanism in the constituent quark model.

2.2 WACS Kinematics

The kinematical requirement for the applicability of the handbag approach is that the Mandelstam variables s, t and u are large compared to a typical hadronic scale of order $\Lambda^2 = 1$ GeV^2 . This implies s, t, $u >> m^2$, where m is the proton mass. For much of the theory and models that rely on the handbag a wide-angle, where $t \sim u > 2.5$ GeV^2 is also preferred. In the SCET framework the observables can only be understood in this large angle kinematic range. For a u smaller than 2.5 GeV^2 no sensible prediction can be made. This is because in the backward kinematics the underlying scattering mechanism is different and in the limited theory for this region effects are already known to have a strong impact.

The external kinematics is determined by the beam energy E_L^γ in the laboratory and the center of mass scattering angle θ. These can then be used to express the invariant Mandelstam variable as,

$$\begin{aligned} s &= 2mE_L^\gamma + m^2, \\ t &= -\frac{s}{2}\left(1-\cos\theta\right)\left(1-m^2/s\right)^2, \\ u &= 2m^2 - s - t. \end{aligned} \qquad (1)$$

2.3 Soft-collinear Effective Theory

Recently a complete factorization formula for the leading power contribution in wide angle Compton scattering has been developed [19, 21]. The soft-spectator contribution describes the scattering which involves the soft modes and resulting soft-spectator scattering contribution to the overall amplitude. The soft collinear effective theory is used in order to define this contribution in a field theoretical approach. The SCET framework is then used to provide a proof of the factorization formula.

The SCET framework permits the implementation of some specific corrections which are related to the soft-overlap contribution. There are indications that numerical effect of this contribution can be dominant at some moderate values of the Mandelstam variables. In general, SCET give a very solid description in the region where the other power corrections are small.

The SCET formalism follows the same idea as in the standard factorization approach, short and long distance physics are factorized separately. The only required assumptions are very general such as that soft partons have soft momenta of order Λ_{qcd}. There is not an additional need to constrain the virtualities by hand. The advantage of SCET formalism is a systematic approach to the factorization of the hard and soft subprocesses.

The asymmetry K_{LL} is studied with the approximation that the hard-spectator contributions are small. Neglecting all power corrections and using the next-to-leading expressions some numerical results as a function of the scattering angle θ are obtained (see Fig.2). The solid red line corresponds to the leading-order approximation. The dashed (blue) and dotted (black) lines show the numerical results for the complete NLO expression for the energies $s = 6.9$ GeV^2 and $s = 20$ GeV^2, respectively. The data points are from experiments E99-114 and E07-002 corresponding to $s = 6.9$ GeV^2 and $s = 7.8$ GeV^2, respectively. The value of the longitudinal asymmetry K_{LL} is qualitatively different from the one that can be obtained in the hard-spectator (hard two-gluon exchange) factorization picture. Calculations have been performed in SCET [18, 22] on the relationship between K_{LL} and A_{LL} using the small contributions from the helicity flip amplitudes and for the wide-angle kinematics leading to $K_{LL} \sim A_{LL}$. Using only the leading order approximations the calculation shows a very weak s-dependence leading to $K_{LL}(s = 9, \theta) \simeq A_{LL}(s = 8, \theta)$ within the theoretical errors. The longitudinal asymmetry A_{LL} as a function of scattering angle θ is shown in Fig. 3. The figure shows a comparison using $s = 8$ GeV^2, $s = 9$ GeV^2 and $s = 14$ GeV^2 to the Klein-Nishina asymmetry for massless quarks.

It is very relevant to describe a factorization for the helicity flip amplitudes but the modeling will be dependent on the new unknown nonperturbative matrix elements. Any experimental data on A_{LL} directly can provide the needed information to move forward in the acquisition of these nonperturbative quantities. At present we have only two points for K_{LL}. One of them (the E99-114 measurement) is at low $|u|$, with the second measurement contradicting predictions from all theoretical approaches. In order to resolve this situation

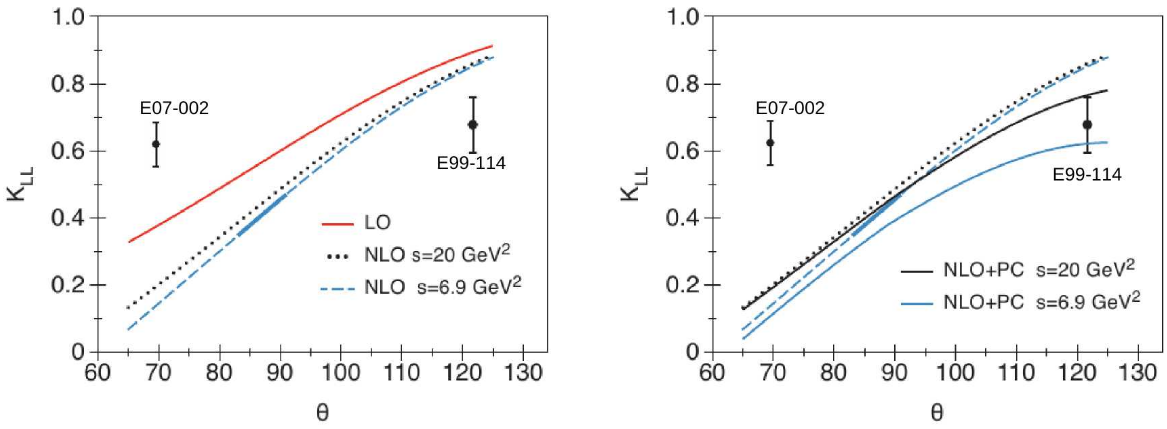

Figure 2: The longitudinal asymmetry K_{LL} as a function of scattering angle θ. (Left) A comparison of the LO (red) and NLO calculated with $s = 6.9$ GeV^2 (dashed) and $s = 20$ GeV^2 (dotted) lines. (Right) A comparison of the NLO results calculated with (solid black) and without (blue line) kinematical power corrections. The massless approximation is the same for both plots [21].

we need measurements in the relevant kinematical region ($t \sim u > 2.5$ GeV^2). Measurements of the same angle at different s can help constrain the scale of the corrections. The GPD model and SCET approach predict that $K_{LL} = K_{LL}^{KN}$ at LO in the Klein-Nishina asymmetry. This implies not only specific angular behavior but also independence on s. In the SCET framework there are also α_s corrections which induce a weak logarithmic dependence. Calculations have been made [21] that compute the NLO corrections. Hence the measurements at the same angle and different s allow one to check the expected theoretical prediction and to make a conclusion about our understanding of the underlying scattering of quarks.

2.4 pQCD Mechanism

The traditional framework for the interpretation of hard exclusive reactions in the asymptotic regime is perturbative QCD (pQCD) [27, 28]. The onset of scaling in Deep Inelastic Scattering (DIS) at the relative low scale of $Q^2 \sim 1$–2 (GeV/c)^2, gives rise to the expectation that pQCD might also be applicable to exclusive processes in the range of a few (GeV/c)^2. pQCD confronts RCS [29, 30, 3] as shown in Fig. 4, where it is seen that the three valence quarks are active participants in the hard subprocess, which is mediated by the exchange of two hard gluons. The soft physics is contained in the valence quark distribution amplitudes. The pQCD mechanism leads naturally to the constituent counting rules for exclusive processes:

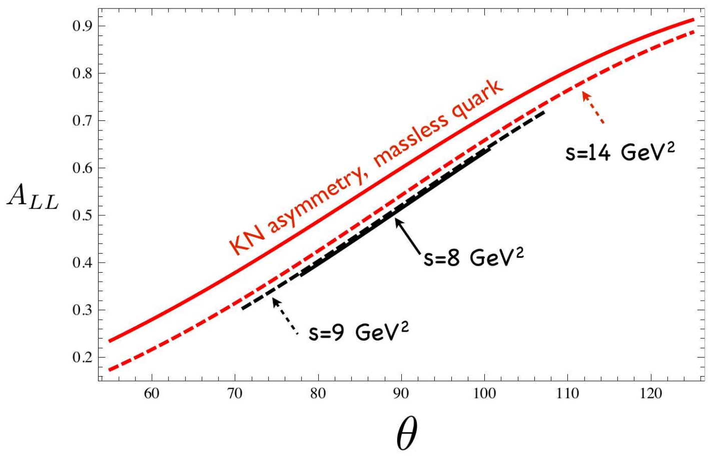

Figure 3: The longitudinal asymmetry A_{LL} as a function of scattering angle θ. A comparison to show the weak s dependence using $s = 8$ GeV^2, $s = 9$ GeV^2 and $s = 14$ GeV^2. Also shown is the Klein-Nishina asymmetry for massless quarks [18, 22].

$$\frac{d\sigma}{dt} \quad = \quad \frac{f(\theta_{cm})}{s^n}\,, \tag{2}$$

where n is related to the number of active constituents in the reaction and $f(\theta_{cm})$ is a function only of the center of mass scattering angle[1, 2]. Indeed, the observation that many exclusive reactions, such as elastic electron scattering, pion photoproduction, and RCS, approximately obey Eq. 2 has led to the belief that the pQCD mechanism dominates at experimentally accessible energies. There seems to be little theoretical disagreement that the pQCD mechanism dominates at sufficiently high energies [27]; however, there is no consensus on how high is "sufficiently high." Despite the observed scaling, absolute cross sections calculated using the pQCD framework are very often low compared to existing experimental data, sometimes by more than an order of magnitude [3, 4]. Moreover, several recent JLab experiments that measure polarization observables also disagree with the predictions of pQCD. In the G_E^p experiment [5, 6, 7] the slow falloff of the Pauli form factor $F_2(Q^2)$ up to Q^2 of 8.5 (GeV/c)^2 provides direct evidence that hadron helicity is not conserved, contrary to predictions of pQCD. Similar findings were made in the π^0 photoproduction experiment [31], where both the non-zero transverse and normal components of polarization of the recoil proton are indicative of hadron helicity-flip, which is again contrary to the predictions of pQCD. Finally, in the recently completed RCS experiment, E99-114 and E07-002, the longitudinal polarization transfer K_{LL} (which will be defined precisely in the next section) shows values which are large and positive, contrary to the pQCD prediction which is small and negative [3]. For all these reasons, it can be argued that pQCD is not the correct mechanism for interpreting exclusive reactions at currently accessible energies and instead we should seek a description in terms of the handbag mechanism. The pQCD calculations predict that A_{LL}=K_{LL}, so a measurement of A_{LL} in combination with the already obtained result for K_{LL} could provide an additional test of pQCD applicability in the JLab energy regime.

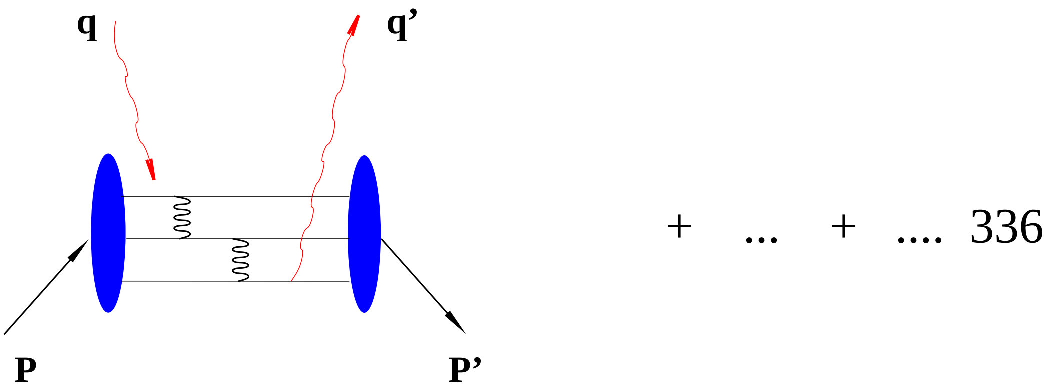

Figure 4: Two gluon exchange pQCD diagram for RCS. 336 diagrams can contribute.

2.5 Handbag Mechanism

The handbag mechanism offers new possibilities for the interpretation of hard exclusive reactions. For example, it provides the framework for the interpretation of deep exclusive reactions, which are reactions initiated by a high-Q^2 virtual photon. The application of the formalism to RCS (see Fig. 5) was initially worked out to leading order (LO) by Radyushkin [10] and subsequently by Diehl *et al.*[11]. The next-to-leading-order (NLO) contributions have been worked out by Huang *et al.*[12]. The corresponding diagram for elastic electron scattering is similar to Fig. 5, except that there is only one external virtual photon rather than two real photons. In the handbag approach, the hard physics is contained in the scattering from a single active quark and is calculable using pQCD and QED: it is just Compton scattering from a structureless spin-1/2 particle.

The soft physics is contained in the wave function describing how the active quark couples to the proton. This coupling is described in terms of GPD's. The GPD's have been the subject of intense experimental and theoretical activity [16, 17]. They represent "superstructures" of the proton, from which are derived other measurable structure functions, such as parton distribution functions (PDF) and form factors (F_1 and F_2). To NLO, only three of the four GPD's contribute to the RCS process: $H(x, \xi = 0, t)$, $\hat{H}(x, \xi = 0, t)$, and $E(x, \xi = 0, t)$. Since the photons are both real, the skewness parameter ξ is zero, reflecting the fact that the

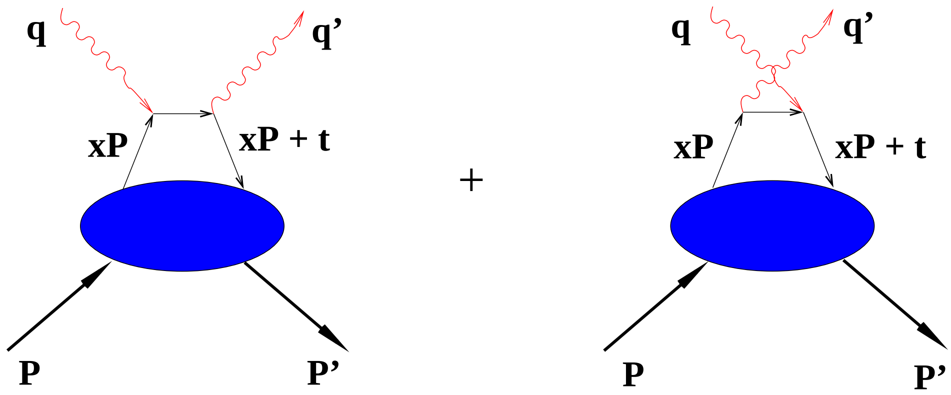

Figure 5: The handbag diagram for RCS.

momentum absorbed by the struck quark is purely transverse. In the handbag formalism, the RCS observables are new form factors of the proton that are x^{-1}-moments of the GPD's:

$$\begin{aligned}
R_{V}(t) &= \sum_a e_a^2 \int_{-1}^{1} \frac{dx}{x} H^a(x,0,t), \\
R_{A}(t) &= \sum_a e_a^2 \int_{-1}^{1} \frac{dx}{x} \operatorname{sign}(x)\, \hat{H}^a(x,0,t), \\
R_{T}(t) &= \sum_a e_a^2 \int_{-1}^{1} \frac{dx}{x} E^a(x,0,t),
\end{aligned}$$

where e_a is the charge of the active quark and the three form factors are, respectively, the vector, axial vector, and tensor form factors. (sign(x) is the sign of x $\equiv \frac{x}{|x|}$.) The corresponding form factors for elastic electron or neutrino scattering are given by the first (x^0) moments of the same GPD's:

$$\begin{aligned}
F_{1}(t) &= \sum_a e_a \int_{-1}^{1} dx\, H^a(x,0,t), \\
G_{A}(t) &= \sum_a \int_{-1}^{1} dx\, \operatorname{sign}(x)\, \hat{H}^a(x,0,t), \\
F_{2}(t) &= \sum_a e_a \int_{-1}^{1} dx\, E^a(x,0,t),
\end{aligned}$$

where the three quantities are, respectively, the Dirac, axial, and Pauli form factors. On the other hand, the $t = 0$ limit of the GPD's produce the PDF's:

$$
\begin{aligned}
H^a(x,0,0) &= q^a(x), \\
\hat{H}^a(x,0,0) &= \Delta q^a(x) \\
E^a(x,0,0) &= 2\frac{J^a(x)}{x} - q^a(x),
\end{aligned}
\tag{3}
$$

where J^a is the total angular momentum of a quark of flavor a and is not directly measurable in DIS.

In the handbag factorization scheme, the RCS helicity amplitudes are related to the form factors by

$$
\begin{aligned}
M_{\mu'+,\mu+}(s,t) &= 2\pi\alpha_{em}\left[T_{\mu'+,\mu+}(s,t)(R_V(t)+R_A(t)) + T_{\mu'-,\mu-}(s,t)(R_V(t)-R_A(t))\right], \quad (4) \\
M_{\mu'-,\mu+}(s,t) &= 2\pi\alpha_{em}\frac{\sqrt{-t}}{m}\left[T_{\mu'+,\mu+}(s,t) + T_{\mu'-,\mu-}(s,t)\right] R_T(t),
\end{aligned}
$$

where μ, μ' denote the helicity of the incoming and outgoing photons, respectively. The signs on M and T refer to the helicities of the proton and active quark, respectively. This structure of the helicity amplitudes leads to a simple interpretation of the RCS form factors: $R_V \pm R_A$ is the response of the proton to the emission and reabsorption of quarks with helicity in the same/opposite direction of the proton helicity, and R_T is directly related to the proton helicity-flip amplitude [12]. These equations leads to expressions relating RCS observables to the form factors.

The most important of these experimentally are the spin-averaged cross section, the recoil polarization observables and A_{LL}. The spin-averaged cross section factorizes into a simple product of the Klein-Nishina (KN) cross section describing the hard scattering from a single quark, and a sum of form factors depending only on t [10, 11]:

$$
\frac{d\sigma/dt}{d\sigma_{\mathrm{KN}}/dt} = f_V\left[R_V^2(t) + \frac{-t}{4m^2}R_T^2(t)\right] + (1-f_V)R_A^2(t)\,. \tag{5}
$$

For the interesting region of large $p_\perp$, the kinematic factor f_V is always close to 1. Consequently the unpolarized cross sections are largely insensitive to R_A, and the left-hand-side of Eq. 5 is nearly s-independent at fixed t. One of the primary goals of E99-114 was to test this relationship as well as to determine the vector form factor R_V. Calculations to NLO, which take into account both photon and proton helicity-flip amplitudes, do not change this prediction in any appreciable way [12, 32]. Updated cross section and Compton form factors (see Fig. 6) with their parametric uncertainties have also been evaluated [24].

The longitudinal and transverse polarization transfer observables, K_{LL} and K_{LS}, respectively, are defined by

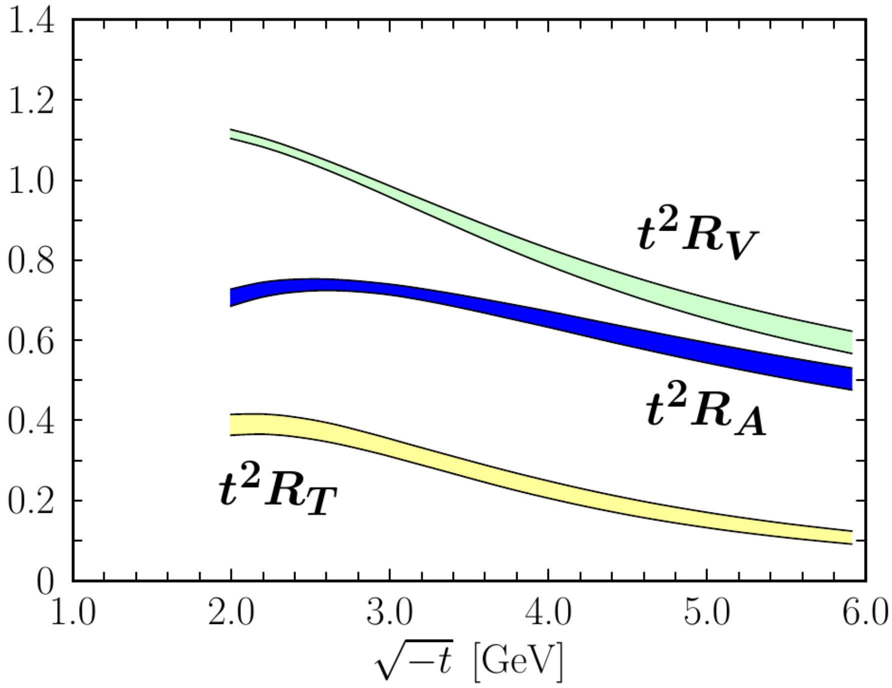

Figure 6: Predictions for the Compton form factors evaluated from the M. Diehl, P. Kroll default fit from Ref. [12], scaled by t^2 and shown in units of GeV^4. The bands in each case show the parametric uncertainties.

$$K_{LL}\frac{d\sigma}{dt} \equiv \frac{1}{2}\left[\frac{d\sigma(\uparrow\uparrow)}{dt} - \frac{d\sigma((\downarrow\uparrow)}{dt}\right] \qquad K_{LS}\frac{d\sigma}{dt} \equiv \frac{1}{2}\left[\frac{d\sigma(\uparrow\rightarrow)}{dt} - \frac{d\sigma(\downarrow\rightarrow)}{dt}\right] \tag{6}$$

where the first arrow refers to the incident photon helicity and the second to the recoil proton helicity ($\uparrow$) or transverse polarization ($\rightarrow$).

With definitions of two additional parameters,

$$\beta = \frac{2m}{\sqrt{s}}\frac{\sqrt{-t}}{\sqrt{s}+\sqrt{-u}} \qquad \kappa(t) = \frac{\sqrt{-t}}{2m}\frac{R_T(t)}{R_V(t)}\,, \tag{7}$$

the three polarization observables are approximately related to the form factors by the expressions [11, 12],

$$K_{LL} \approx K_{LL}^{\rm KN}\frac{R_A(t)}{R_V(t)}\frac{1-\beta\kappa(t)}{1+\kappa^2(t)} \qquad \frac{K_{LS}}{K_{LL}} \approx \kappa(t)\frac{1+\beta\kappa^{-1}(t)}{1-\beta\kappa(t)} \qquad P_N \approx 0\,, \tag{8}$$

where K_{LL}^{KN} is the longitudinal asymmetry for a structureless Dirac particle. These formulas do not include small gluonic corrections, which are discussed in Ref. [12].

The expressions above show that measurements of K_{LL} and K_{LS}, when combined with measurements of $d\sigma/dt$, allow determinations of all three form factors. They also show that two very important pieces of information follow directly from the spin asymmetries: K_{LL} and K_{LS} / K_{LL}, which are directly related to the form factor ratios R_A/R_V and R_T/R_V, respectively. For large energies and scattering angles near $\theta_\gamma^{cm}= 90°$, the β terms are negligible small so the measurements more direct [12].

The initial state helicity correlation parameter is defined by,

$$A_{LL}\frac{d\sigma}{dt} \equiv \frac{1}{2}\left[\frac{d\sigma(\uparrow\uparrow)}{dt} - \frac{d\sigma((\downarrow\uparrow)}{dt}\right] \tag{9}$$

where the first arrow refers to the incident photon helicity and the second to the initial state proton helicity ($\uparrow$). In the GPD approach of Ref. [12], the initial state helicity correlation parameter, A_{LL}, is predicted to be equivalent to K_{LL} if this can be shown to be true then all the relationships between A_{LL} and the RCS form factors are the same as shown above for K_{LL}.

From the relationships (Eq. 3) connecting the RCS form factors to PDFs, the ratio R_A/R_V is related to $\Delta q^a(x)/q^a(x)$. For RCS, the e_a^2-weighting of the quark flavors means that u quarks will dominate the reaction. Moreover, at relatively large $-t$, the contributions to the form-factor integral are concentrated at moderate-to-high x, where the valence quarks dominate. Therefore, the A_{LL} asymmetry contains direct information on $\Delta u(x)/u(x)$ in the valence region. We propose to investigate this in the present experiment, up to $-t = 5.4$ (GeV/c)^2.

Obtaining this kind of information is one of the key physics elements justifying the 12 GeV upgrade of JLab. From the correspondence between RCS and electron scattering form factors, there is expected to be a close relationship between R_T/R_V and F_2/F_1 [12]. The measurements of G_E^p at JLab [5, 6, 7] have shown that F_2/F_1 falls as $1/\sqrt{-t}$ rather than as $1/t$, the latter being predicted by pQCD. It will be an important check on the theoretical interpretation of F_2/F_1 to see if R_T/R_V behaves in a similar way. The results from E99-114 at $-t = 4$ are large but suggest that the R_T/R_V may fall more rapidly with $-t$ than F_2/F_1. Experiment E07-002 has obtained better precision on K_{LT} and K_{LL}, but its kinematic limitations make it difficult to say anything definite about the relationship between F_2/F_1 and R_T/R_V. These results must be compared with the R_T/R_V acquired with the A_{LS} and A_{LL} asymmetries. This will serve as a consistency check if K_{LL} and A_{LL} are equal, but serve as a phenomenological basis if they are not. It is expected that significant model sensitivities occur in beam-target double-polarization asymmetries, these could be measured with much higher efficiency than ones requiring recoil polarization determination.

2.5.1 Relating Spin Dependent Observables in the Handbag Approach

The center of mass helicity amplitudes $\Phi_{\mu\nu',\mu\nu}$ are obtained from the light-cone helicity amplitudes (as taken from [12]), defined in the symmetric frame,

$$\Phi_{\mu'\nu',\mu\nu} = \mathcal{M}_{\mu'\nu',\mu\nu} + \beta/2\left[(-1)^{1/2-\mu'}\mathcal{M}_{\mu'-\nu',\mu\nu} + (-1)^{1/2+\mu}\mathcal{M}_{\mu'\nu',\mu-\nu}\right] + \mathcal{O}\left(\Lambda^2/t\right). \quad (10)$$

The generic notation for the six independent helicity amplitudes can be expressed as,

$$\Phi_1 = \Phi_{++++},\ \Phi_3 = \Phi_{-+++},\ \Phi_5 = \Phi_{+-+-}, \quad (11)$$

$$\Phi_2 = \Phi_{--++},\ \Phi_4 = \Phi_{+-++},\ \Phi_6 = \Phi_{-++-}. \quad (12)$$

Inspection of Eq. 5 and Eq. 10 leads to

$$\Phi_2 = -\Phi_6 + \mathcal{O}\left(\Lambda^2/t\right), \quad (13)$$

within this [12] handbag approach where the amplitudes Φ_2, Φ_3, Φ_6 are of order α_s. Then in the convention of Bourrely, Leader and Soffer [14] the three different polarization states of the proton can be considered. The bases L, S, and N are difined as spin eigenstates of $\mathbf{A}\cdot\sigma$ where σ is the vector of Pauli matricies and $\mathbf{A}$ is any of the unit vectors

$$\mathbf{L}^{(')} = \frac{\mathbf{p}^{(')}}{|\mathbf{p}^{(')}|}, \quad \mathbf{N} = \mathbf{L}\times\mathbf{L}', \quad \mathbf{S}^{(')} = \mathbf{N}\times\mathbf{L}^{(')}. \quad (14)$$

Where $\mathbf{p}$ and $\mathbf{p}'$ are the three-momenta of the incoming and outgoing protons, respectively. For longitudinal polarization observables there are the two-spin correlations of which the helicity (L-type) correlations and how they relate to each other are of particular interest. The longitudinally polarized target observable A_{LL} can be expressed as,

$$\begin{aligned} A_{LL}\frac{d\sigma}{dt} &= \frac{1}{32\pi(s-m^2)^2}\left[|\Phi_1|^2 + |\Phi_2|^2 - |\Phi_5|^2 - |\Phi_6|^2\right] \quad (15)\\ &= \frac{\pi\alpha_{em}^2}{2(s-m^2)^2}R_A\Big\{R_V\left[1-\beta_\kappa\right]\left[|\mathcal{H}_{++++}|^2 - |\mathcal{H}_{+-+-}|^2\right] \\ &\quad +R_V^g\left(\mathcal{H}^{LO}_{++++} - \mathcal{H}^{LO}_{+-+-}\right)\mathrm{Re}\left(\mathcal{H}^g_{++++} + \mathcal{H}^g_{+-+-}\right)\Big\}. \end{aligned}$$

In the models discussed in [12] the $\cos\theta$ dependence of A_{LL} reflects the corresponding helicity correlation for the photon-parton subprocess, $(s^2-u^2)/(s^2+u^2)$, diluted by the form factors. This observable can be compared to the correlation between the helicities of the incoming photon and the outgoing proton,

$$K_{LL}\frac{d\sigma}{dt} = \frac{1}{32\pi(s-m^2)^2}\left[|\Phi_1|^2 - |\Phi_2|^2 - |\Phi_5|^2 + |\Phi_6|^2\right], \quad (16)$$

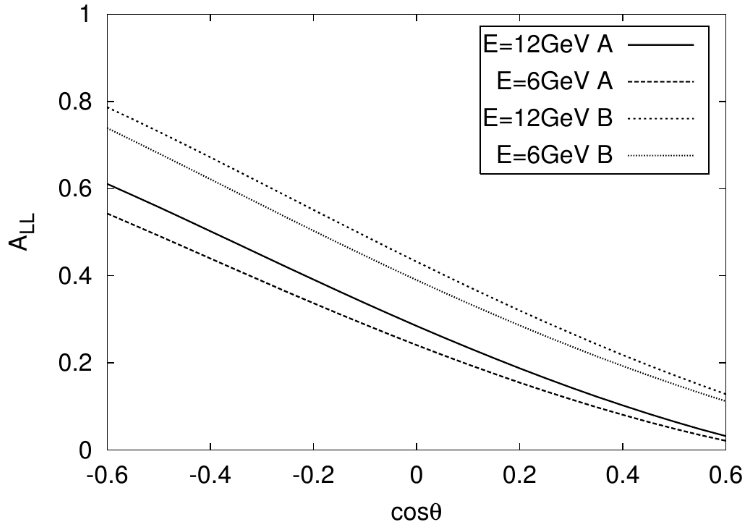

Figure 7: Predictions for the initial state helicity correlation A_{LL} for the two scenarios discussed in [12] at photon lab energies of 6 GeV and 12 GeV.

and since $\Phi_2 = -\Phi_6$ in the handbag approach, [12], we can write

$$A_{LL} = K_{LL}.$$

The transverse polarized target can be used to extract the sideway proton spin directions. The correlation between the helicity of the incoming photon and the sideway (S-type) polarization of the incoming proton, parallel ($\rightarrow$) or antiparallel ($\leftarrow$) to the S-direction reads

$$\begin{aligned} A_{LS}\frac{d\sigma}{dt} &= \frac{1}{2}\left[\frac{d\sigma(\uparrow\rightarrow)}{dt} - \frac{d\sigma(\downarrow\rightarrow)}{dt}\right] \qquad (17)\\ &= \frac{1}{16\pi(s-m^2)^2}\mathrm{Re}\left[(\Phi_1-\Phi_5)\Phi_4^* - (\Phi_2+\Phi_6)\Phi_3^*\right] \\ &= -\frac{\pi\alpha_{em}^2}{2(s-m^2)^2}R_A\left\{\frac{\sqrt{-t}}{2m}R_T\left[1+\beta_\kappa^- 1\right]\left[|\mathcal{H}_{++++}|^2 - |\mathcal{H}_{+-+-}|^2\right]\right. \\ &\quad \left. +\beta R_V^g\left(\mathcal{H}_{++++}^{LO} - \mathcal{H}_{+-+-}^{LO}\right)\mathrm{Re}\left(\mathcal{H}_{++++}^g + \mathcal{H}_{+-+-}^g\right)\right\} \end{aligned}$$

In the same handbag approach unlike A_{LL} the observable A_{LS} is predicted to be relatively independent of photon energy (see Fig. 8) but considerably sensative to the form factor R_T. The correlation between the helicity of the incoming photon and the sideway polarization of

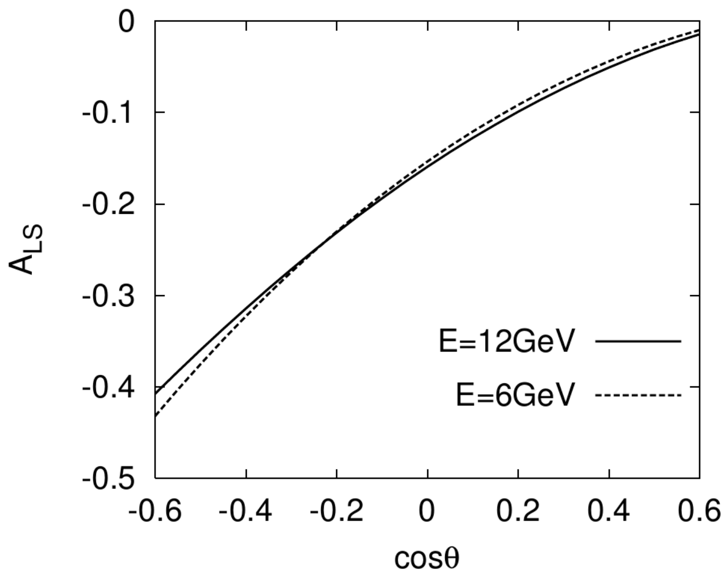

Figure 8: Predictions for the correlation A_{LS} at photon lab energies of 6 GeV and 12 GeV [12].

the outgoing proton is expressed as

$$K_{LS}\frac{d\sigma}{dt} \quad = \quad \frac{1}{16\pi(s-m^2)^2}\mathrm{Re}\left[(\Phi_1-\Phi_5)\Phi_4^* + (\Phi_2+\Phi_6)\Phi_3^*\right].$$

Due to the equivalance $\Phi_2 = -\Phi_6$ the two sideways polarization observables can be related such that

$$A_{LS} = -K_{LS}.$$

Under the standard handbag approach a measurement of both A_{LL} and A_{LS} at the same kinematics is very powerful as one can extract the Compton form factors R_A and R_T from the data with completely different observables not yet measured while establishing the relationship between the other observables. This would not only provide a crucial test of the handbag approach but also help in improving the parameterizations of the corresponding GPDs $\tilde{H}$ and E, respectively. The experimental measurements of K_{LS} are in agreement within the experimental uncertainties with calculations for both the leading-quark and the pQCD approaches [30, 12, 25, 19, 20] suggesting that there is no strong evidence for proton helicity flip in this reaction. The measurements indicate that there is good reason to think that our understanding of K_{LS} is correct over θ_γ^{cm}. Using this understanding, any measurements of A_{LS} can help to confirm the relationship between A_{LS} and K_{LS} without direct kinematic overlap (though our proposed θ_γ^{cm}=120° has direct angle overlap for A_{LS} and previously measured K_{LS}). The experimental results for K_{LS} are $K_{LS}(s = 7.8, \theta_{cm} = 70) = -0.089 \pm 0.071$ and

$K_{LS}(s = 6.9, \theta_{cm} = 120) = 0.114 \pm 0.087$. If the measurements result in something again completely unexpected these results will be used to develop a new understanding using the phenomenology observed.

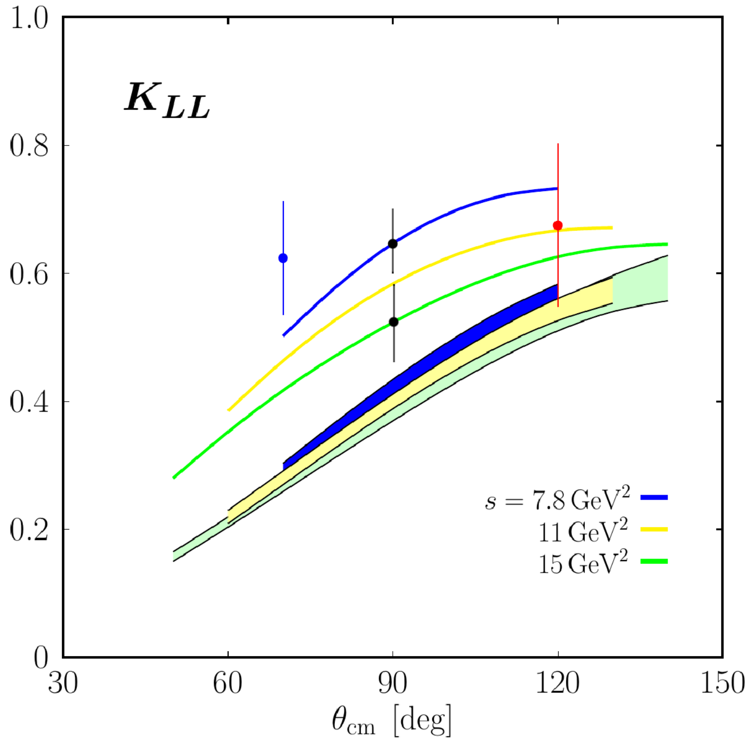

Figure 9: An example fit used in the hangbag approach to the data on the axial form factor and the two K_{LL} measured data points. The new results are indicated by the lines and the old predictions are indicated by the bands [13]. The results of the K_{LL} measurment from E02-007 are shown as the blue point and from E99-114 as the red point. Our proposed measurements at θ_γ^{cm}=90° are shown as the black points for 4.4 GeV and 8.8 GeV electron beam energy.

The uncertainties of the axial form factor R_A is particularly large due to the very limited accuracy of the data. Moreover this form factor is known only at rather low values of $-t$. This is perhaps the reason for the discrepancy between the new K_{LL} measurement and our predictions. In Fig. 9 an example [13] is shown of a handbag model fit to the data on the axial form factor and the two data points on K_{LL}. Significant improvements to this model can be made with additional measurements since not only is the axial form factor data poor but the K_{LL} data used hardly respect the kinematical requirement of the handbag approach s, $-t$, $-u >> m^2$. Our proposed measurements at θ_γ^{cm}=90° are also included, shown as the black points for 4.4 GeV and 8.8 GeV electron beam energy. As seen from the curves (as compared to the previous results shown as bands), it is possible to obtain a result close to the K_{LL} data. Clearly additional measurements are needed that optimized the amount of information acquired while satisfying the kinematic requirements.

2.6 Relativistic constituent quark model for RCS

The relativistic constituent quark model developed by G. A. Miller [25] addresses the question of what is the dominant reaction mechanism that allows the proton to accommodate the large momentum transfer in exclusive reactions such as elastic electron and photon scattering. This model has been successful in describing the electromagnetic nucleon form factors [33]. Unlike the handbag calculations within the GPD approach [11, 12], Miller's model does not neglect quark and hadron helicity flip. The model starts with a wave function for three relativistic constituent quarks:

$$\Psi(p_i) = u(p_1)u(p_2)u(p_3)\psi(p_1, p_2, p_3),$$

where p_i represents space, spin, and isospin indices. It evaluates the wave function in the light cone variables and the calculations are relativistic. They obey gauge invariance, parity conservation, and time reversal invariance. They include quark mass effects and proton helicity flip. Due to lower components of Dirac spinors, where the quark spin is opposite to that of the proton, quark orbital angular momentum appears. The resulting predictions for the polarization observables A_{LL} and K_{LL} and the cross section are shown in Fig. 10 and Fig. 11, together with data from the E99-114 experiment. The most striking consequence of Miller's results is a big difference between A_{LL} and K_{LL} at large scattering angles, which we can test experimentally.

2.7 Polarization in QED Compton process

It is instructive to evaluate polarization effects in the QED process $e\gamma \to e\gamma$. The Klein-Nishina process is an example that is fully calculable and which plays a major role in RCS, when the handbag diagram dominates. It is useful to evaluate polarization observables for different ratios of the electron mass to the photon energy.

Polarization observables in QED are given in invariant variables as [34] :

$$A_{LL}^{KN} = \left[-\frac{s-m^2}{u-m^2} + \frac{u-m^2}{s-m^2} - \frac{2m^2t^2(s-u)}{(s-m^2)^2(u-m^2)^2}\right] / \left[-\frac{s-m^2}{u-m^2} - \frac{u-m^2}{s-m^2} + \frac{4m^2t(m^4-su)}{(s-m^2)^2(u-m^2)^2}\right]$$

$$K_{LL}^{KN} = \left[-\frac{s-m^2}{u-m^2} + \frac{u-m^2}{s-m^2} - \frac{4m^2t^2(m^4-su)}{(s-m^2)^3(u-m^2)^2}\right] / \left[-\frac{s-m^2}{u-m^2} - \frac{u-m^2}{s-m^2} + \frac{4m^2t(m^4-su)}{(s-m^2)^2(u-m^2)^2}\right]$$

Fig. 12 shows the A_{LL}^{KN} and K_{LL}^{KN} for different energies of the incident photon as a function of the scattering angle in the *lab*. At low t/s and for $m/E_\gamma << 1$ the difference between K_{LL} and A_{LL} vanishes. At $\theta_{lab} = \pi/2$ the observable A_{LL}=0. In the limit $m/E_\gamma \to 0$

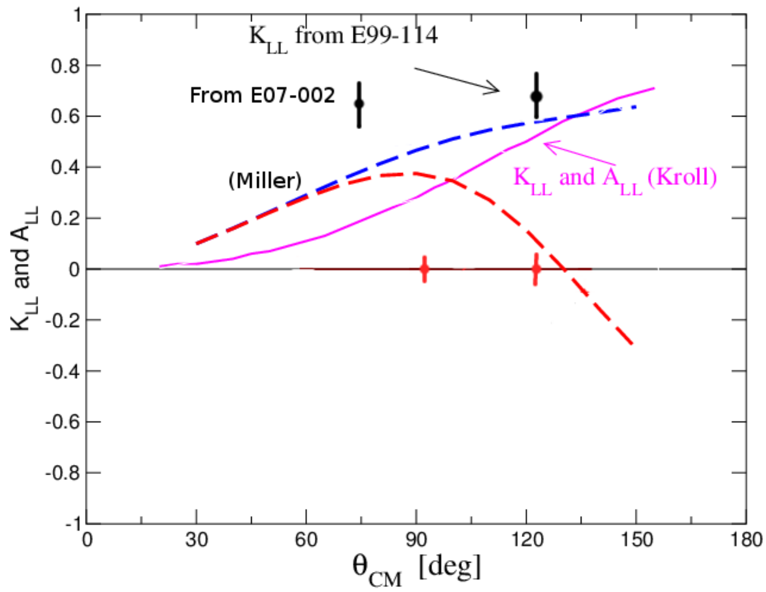

Figure 10: Predictions for A_{LL} in the GPD approach of (Kroll) Ref. [12] and CQM of (Miller) Ref. [25] shown as the split line along with the data on K_{LL} from E99-114 and E07-002 (points in black) and the projection of two of the proposed points (points in red) with one of the proposed points for A_{LL} overlapping at θ_γ^{cm}=120° with the K_{LL} data point from E99-114.

A_{LL}=K_{LL} for all values of θ_γ not equal to 180°. At $\theta_\gamma = 180°$ the value of $A_{LL} \approx -K_{LL}$. If we now look at Miller's calculation (see Figure 10) which has $m/E_\gamma \sim 1/10$ and $\theta_{lab} \approx 90°$ (our kinematics labeled P2, see Table 2) the difference between K_{LL} and A_{LL} is about 0.7.

2.8 Regge Exchange Mechanism

When s, $-t$, and $-u$ are not sufficiently large, then the factorization into hard and soft process may not apply, in which case neither the pQCD nor the handbag approach is valid. An alternative approach has been proposed by Laget [15] based on Vector Meson Dominance (VMD). In the VMD approach, the photon fluctuates into a vector meson, which then interacts with the target via t-channel exchange of mesons (which dominates at low t or forward angles) or u-channel exchange of baryons (which dominates at low u or backward angles). The open question is how high t or u must be in order that the VMD mechanism becomes small compared to the handbag mechanism. The VMD model has had recent successes even at moderately large t. For example the VMD model is able to fit the observed low value of the G_E^p form factor [6] at -t = 5.6 (GeV/c)^2 [35].

Real and Virtual Compton Scattering were studied in a model based on Regge trajectories and two-gluon exchange by F. Cano and J.-M. Laget [15]. The parameters of the model

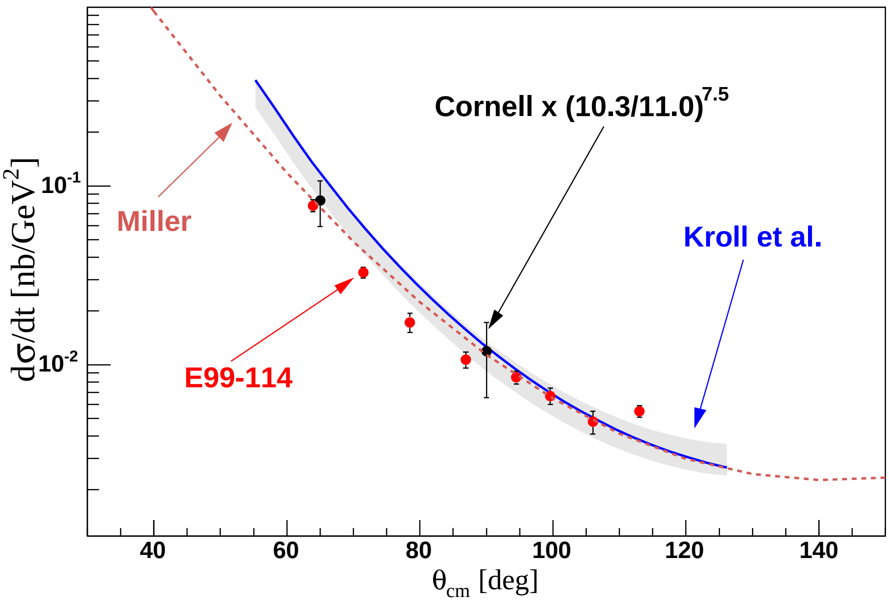

Figure 11: Cross section of RCS process at s = 11 (GeV/c)^2 from E99-114 and Cornell[39] experiments (scaled to the same CM energy) and results of calculations in the GPD approach (Kroll [12]) and from a CQM (Miller [33]).

were "tuned" by fitting data from vector meson photonproduction [36, 37], giving rise to predictions for the cross section and spin observables in RCS involving only a single free parameter, the radiative decay constant of the ρ meson. Given the close agreement over much of the kinematic range between the handbag and VMD predictions, they point out that at presently accessible momentum transfer, the contribution to RCS from the hadronic component of the photon is not negligible (see review [38]). For example the predicted longitudinal polarization transfer (see Fig. 13) $A_{LL}$is positive, close to the prediction of the handbag approach at θ^{cm} below 140°, and close to the result from E99-114. However, it strongly deviates from the handbag prediction at larger angles, where the u-channel exchange of baryons becomes dominant.

2.9 Summary of Motivation

It is important to realize that the issues posed at the start of this section are not limited to the RCS reaction. Indeed, they are questions that need to be addressed by all studies of the proton using exclusive reactions in the hard scattering regime. The old paradigm for addressing these questions was the pQCD mechanism and the distribution amplitudes. It is quite likely that the new paradigm will be the handbag mechanism and GPD's. In any case,

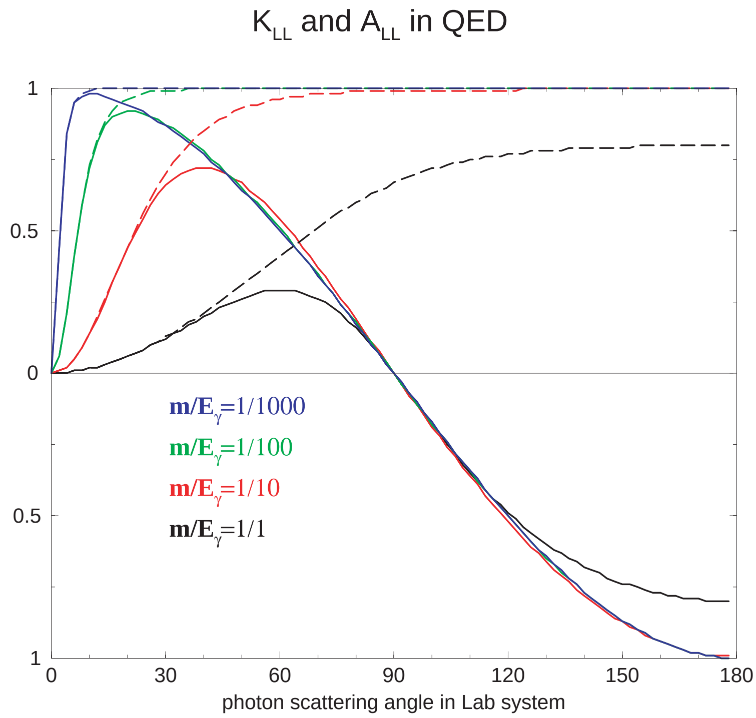

Figure 12: Klein-Nishina polarization observables A_{LL} and K_{LL}, shown by solid lines and dashed lines respectively, for different ratios of the electron mass to the photon energy as a function of the scattering angle in the lab system.

the reaction mechanism needs to be tested, not only over a wide range of kinematic variables but also over a wide range of different reactions. Of these, RCS offers the best possibility to test the mechanism free of complications from additional hadrons. The CQM was quite successful in its description of many observables of the hadronic structure and generates a useful and intuitive picture of the hadron. The proposed test presents a unique case where predictions of the CQM and QCD–based theory are qualitatively different.

The measured values obtained for K_{LL} are larger than expected with the most recent measurement being larger than any available models. Both measurements are in a kinematic range weakly appropriate for prediction to be valid. To best explore the relationship between K_{LL} and A_{LL} it is necessary to look at overlapping kinematics for separate measurements of these polarized observables. In order to test the handbag approach more accurately than previous measurements it is necessary to study A_{LL} within the strict WACS kinematic regime. The most information will come from measurements of A_{LL} at the same s but different t to study the t dependence alone. But also taking data at the same t but different s to measure the s dependence. From the plots showing A_{LL} or K_{LL} there is very distinctly

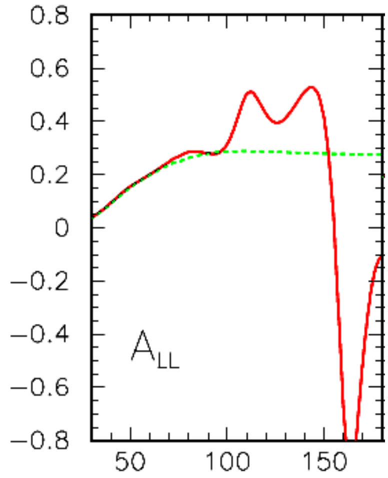

Figure 13: Prediction from [15] of A_{LL} in Compton Scattering at $E_\gamma = 4$ GeV. Dashed lines are the contribution of Regge Exchange in the t-channel. Solid lines are the final results, which include u-channel exchanges.

both s and $\cos\theta$ dependence. The handbag predictions for A_{LS} do not have s dependence so results confirming that would be important. Results indicating otherwise, or something other than what would be expected for K_{LS} at the same kinematics, would be extraordinary. Measuring both A_{LL} and A_{LS} for ideal WACS kinematics at the same points will allow accurate extraction of R_T/R_V. This will help to establish the relationship between F_2/F_1 and R_T/R_V. This would not only provide crucial tests of the handbag approach but also help in improving the parameterizations of the corresponding GPDs $\tilde{H}$ and E, respectively.

2.10 Summary of Physics Goals

We propose measurements of the spin correlation asymmetry A_{LL} at $\theta_\gamma^{cm}= 90°$ at two different incident photon energy of 4.4 GeV, s=8 (GeV/c)^2 and 8.8 GeV, s=15 (GeV/c)^2. We also prosose a measurement of $A_{LL}$and A_{LS} at s=15 (GeV/c)^2 at $\theta_\gamma^{cm} = 120°$ overlapping in θ_γ^{cm} with the K_{LL} and K_{LS} measurement in E99-114. The specific physics goals are as follows:

1. To make a measurement of $A_{LL}$and A_{LS} at large s, t and u where applicability and limitations of GPD based calculations are under control. A high precision measurements with optimized kinematics will support the surprising results for $K_{LL}$from experiment E99-114 [8] and E07-002 [26].

2. To provide a test that can expose, in an unambiguous way, how the RCS reaction pro-

ceeds: either via the interaction of photons with a current quark or, with a constituent quark.

3. To accurately determine the form factor ratio R_A/R_V from the measurement of A_{LS} and A_{LL} and correlate this ratio with the corresponding values of F_2/F_1 determined from elastic electron scattering.

4. Directly test the s-dependence and the anlge dependence of A_{LL} and A_{LS} providing constraints to move the theoretical framework forward while adding to WACS phenomenology by expanding the number of measured polarized observables and kinematic coverage.

The overall statistical precision with which we will address these physics goals will be discussed in Sec. 5.

3 Experimental Setup

The proposed experiment will study the scattering of polarized photons from polarized protons in a NH_3 target, as illustrated in Fig. 14. The Compton scattered photon and the recoiling proton will be detected in the Neutral Particle Spectrometer (NPS) and the High Momentum Spectrometer respectively.

We assume an incident electron beam of 4.4 and 8.8 GeV with intensity of 3μA and 80% polarization. Such currents and polarizations have already been delivered using the strained GaAs source at Jefferson Lab. The target will be a longitudinally polarized proton, the so called UVA/JLAB polarized target, operating in a 5 Tesla field pointing along the beam line (longitudinal) or perpendicular to the beam line (transverse). Any charged particles are swept away by the target field will deflect the charged particles away from the NPS.

With an electron beam of 100na intensity on UVA/JLAB polarized target, a average NH_3 polarization of 75% have been achieved in several experiments, i.e. RSS, SANE experiments in Hall C, g_2^P and G_E^P experiments in Hall A. As we will present a pure photon beam to the target its operation will be simplified and we expect a significantly higher average polarization. The beam polarization will be measured with a systematic uncertainty of 1% with the Hall C Möller polarimeter. The large cross section and helicity asymmetry for π^0 photoproduction, as determined in E99-114, will provide a monitor of the electron beam polarization continuously during data taking at fixed kinematic conditions with large θ_γ^{cm}(See discussion in Section 4.3 on signal extraction).

3.1 The Polarized NH_3 Target

This experiment we will use the UVA/JLAB polarized target, which has been successfully used in E143/E155/E155x experiments at SLAC and E93-026, E01-006, E07-003, E08-007 and E08-027 at JLab. E08-007 and E08-027 used a different superconducting split Helmholtz pair, originally part of the Hall B polarized target. The coil package is very similar to the original one. See Fig. 15 for a cross sectional view. The target polarization will be oriented both longitudinal and transverse (within 5°) to the beam, made necessary for acceptance issues.

This target operates on the principle of Dynamic Nuclear Polarization (DNP). The low temperature (1 K°), high magnetic field (5 T) natural polarization of solid materials (ammonia, lithium hydrides) is enhanced by microwave pumping. The polarized target assembly contains two 3–cm–long target cells that can be selected individually by remote control to be located in the uniform field region of the magnet. They are also 2 other target cells which are available for a calibration target (carbon foil or CH_2). The permeable target cells are immersed in a vessel filled with liquid helium and maintained at 1 K by using a high power evaporation refrigerator. The magnet coils have a 55° conical shaped aperture along the axis

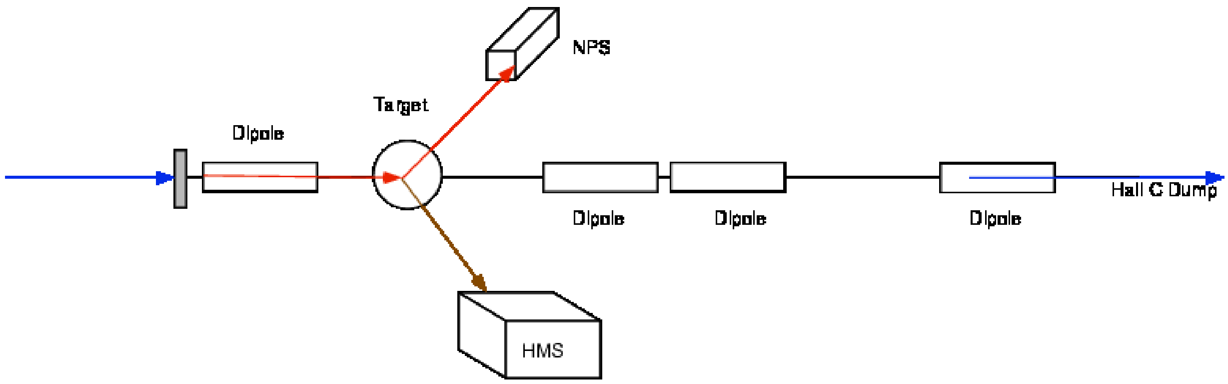

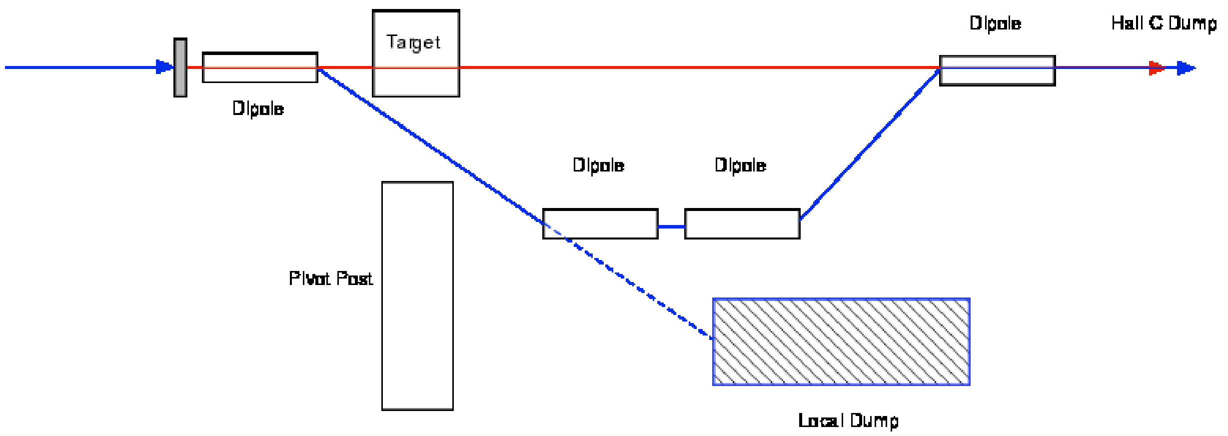

Figure 14: Schematic of the experimental setup. The electron beam comes in from the left and strikes a 6% radiator producing polarized bremsstrahlung photons. Two options for producing the pure photon beam are proposed. In both the electrons are deflected by a dipole just after the radiator and 1) drift to a local dump on the floor of the hall or 2) are delivered to the Hall C dump after passing through 3 more dipoles. Both options are discussed in detail below. The real photon beam interacts with polarized protons in the NH_3 target. The elastically scattered photon is detected in the Neutral Particle Spectrometer and the protons are analyzed in the HMS.

and a 38° wedge shaped aperture along the vertically oriented mid-plane.

The target material is exposed to 140 GHz microwaves to drive the hyperfine transition which aligns the nucleon spins. The DNP technique produces proton polarizations of up to 95% in the NH_3 target. The inexorable fall in polarization due to radiation damage in an electron beam will be markedly reduced with a pure photon beam and we will be able to avoid much of the overhead spent in annealing the radiation damage away. The time spent in this exercise to recover from the radiation damage will be reduced by two-thirds. As part of the program to minimize the sources of systematic errors, the target polarization direction will be reversed after each anneal by adjusting the microwave frequency.

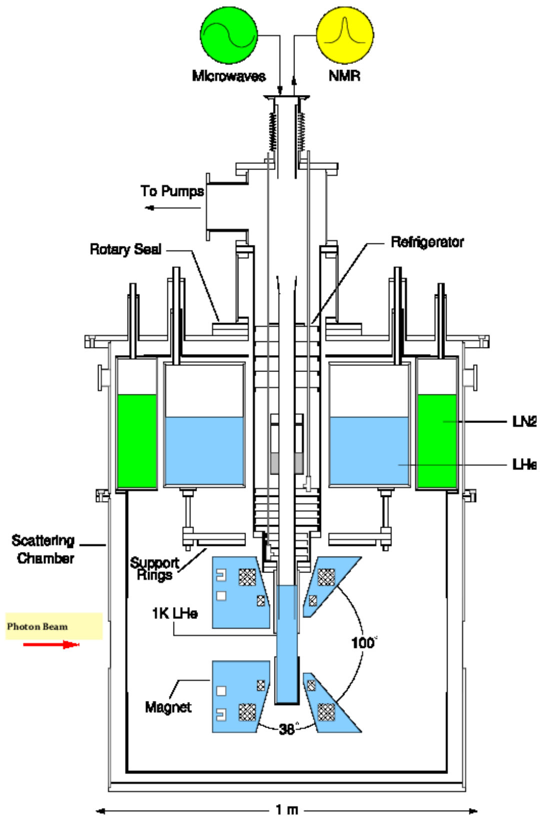

Figure 15: Cross sectional view of the polarized target.

In the case of a mixed electron-photon beam the polarized target field has a very positive effect: it deflects any outgoing charged particles, both the vertically and horizontally greatly improving the selection of the elastically scattered photons at the calorimeter. With a pure photon beam, this becomes irrelevant

3.2 Pure Photon Source

Our 2014 approved experiment E-12-14-006 followed an experiment from the 6 GeV era, E-05-101, that never ran. The benefit of a pure photon beam was appreciated even then and a conceptual plan was presented by D. Day at the Jan 2006 Hall C winter meeting. Removing the electrons after the radiator presents to the target a pure photon beam with much reduced radiation damage and heat load - with a successful scheme one could run the target as usual but gain factors of 10 in FOM. With the approval of E-12-14-006 we returned to this idea in a more concrete way and by October 9, 2014 presented an early concept to place a 2m long dipole just after the radiator to deflect the beam to a local dump in front of the polarized target. Taking this idea further, B Wojtsekhowski, G. Niculescu and collaborators included a Compact Photon Source in their Hall A proposal. The CPS has certain strengths but shared the difficulty of our alternative of a split function (dipole and dump) - a large shielded dump immediately adjacent to the target.

Here, we propose something new, but not radical. We will place a dipole terminating 4 m upstream of the target and immediately after the radiator to deflect the electrons underneath the polarized target can where a gap of 43 cm exists between it and the pivot post. This feature allows two approaches - a single magnet directing the unwanted electrons to a 'local' 27 kW dump (8.8 GeV at 3μA) on the floor by drifting 20 m (or less) or by incorporating three more dipoles to return the beam to the high power Hall C dump.

All the dipoles needed to go back to the dump can be built around the common 2m long FZ's in use at JLAB. This design requires a modified and tapered pole and high current density (833A and 1420 A/cm^2) to produce 2.07 T. If necessary for adequate cooling with LCW under 15 bar, new coils may be procured in addition to the tapered poles. The dipole locations are listed in Table 1.

Table 1: End of dipoles relative to target center (z-position) in cm

Dipole #	Location (cm)
1	-431.4
2	525
3	765
4	1737

Our simulations have been done in G4beamline[1]. G4beamline is a particle tracking simulation program based on Geant4 against which it has been checked. Figure 16 shows the four dipole scheme and the "spray" generated as the beam moves downstream. Neutral particles (photons) are green, electrons are red and positrons are blue. The field map for the dipoles has been generated by OPERA and we include the effects of the polarized target field

[1]http://www.muonsinternal.com/muons3/

as the electrons pass under the can. In longitudinal mode the target provides a small kick in the horizontal direction requiring a small shift of the last dipole in the same direction. In transverse mode, with the field direction on beam left, the deflected beam is moved down by less than a degree, easily compensated by the first dipole. The dipole model includes absorbers between the coils at both the entrance and the exit. There is a photon collimator at the end of the first dipole as well as an absorber. Each of the next three dipoles also have a thick absorber at their entrances. All results were generated using the QGSP-BERT model.

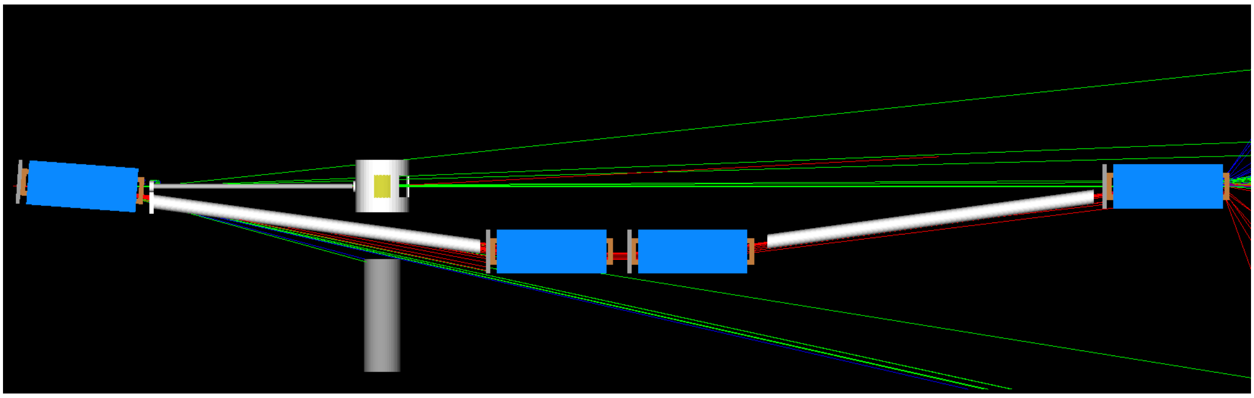

Figure 16: Four dipole scheme to move electrons to the Hall C dump. Here 100 electron events are tracked from the radiator to the exit of the 4th dipole. A 100 MeV cut is imposed. The first dipole is tilted by 5°. Figures 17 and 18 detail where the power is lost along the beam line.

Our study of both schemes are encouraging. In the four dipole case we have found that the limits are imposed by the gap of the FZ's. This is especially evident in dipole four where there is a significant power deposited. Nonetheless we find that 75% of the total beam power can be delivered to the dump. Figure 17 and Figure 18 reveal where the power is lost. One can see that the collimator and absorber for the first dipole and the absorber at the fourth dipole are the primary loss leaders. They will, of course, have to cooled and shielded. The photon collimator will be designed using the lessons learned in developing the PREX electron collimator from Hall A

Figure 19 shows the single dipole scheme which has a telescoping beam pipe from the first dipole to the dump. Fig. 20 illustrates where the power is lost along the way. We have not designed the dump itself but it will share principles of all low power dumps: a copper slug and a tungsten body, water cooled, surrounded by a hermetic steel and concrete chamber.

With electrons, the beam is rastered over the full face of the target cell in order to insure uniform irradiation of the material - this is a requirement in order to have uniform polarization of the material. In turn, knowledge of the beam position on the target face is required for optics reconstruction. With the pure photon beam we must employ a different

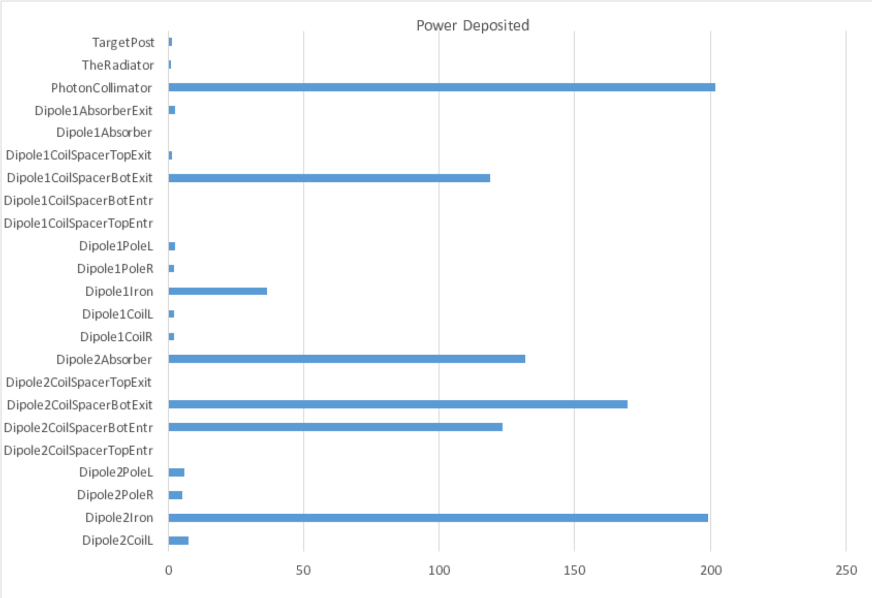

Figure 17: Power lost along beam line with 8.8 GeV, 1 μA beam and a 6% radiator with beam going back to the Hall C dump. The chart should understood by reading from top to bottom (along the path of the electrons) and continuing to the second bar chart in the same order. We find 75% of the beam power is delivered to the dump. The power deposited in target is less than 50mW.

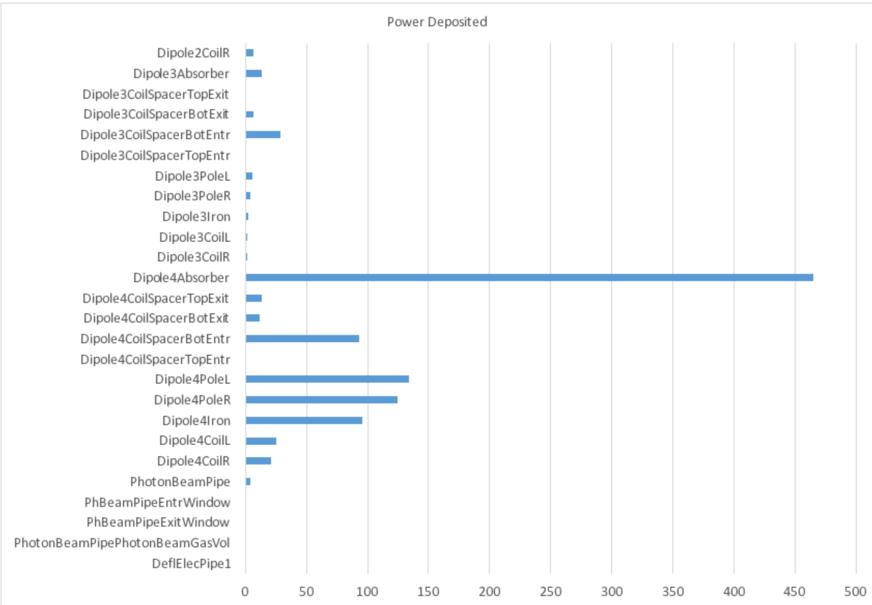

Figure 18: Continuation of chart above. The bar chart should understood by reading from top to bottom (along the path of the electrons).

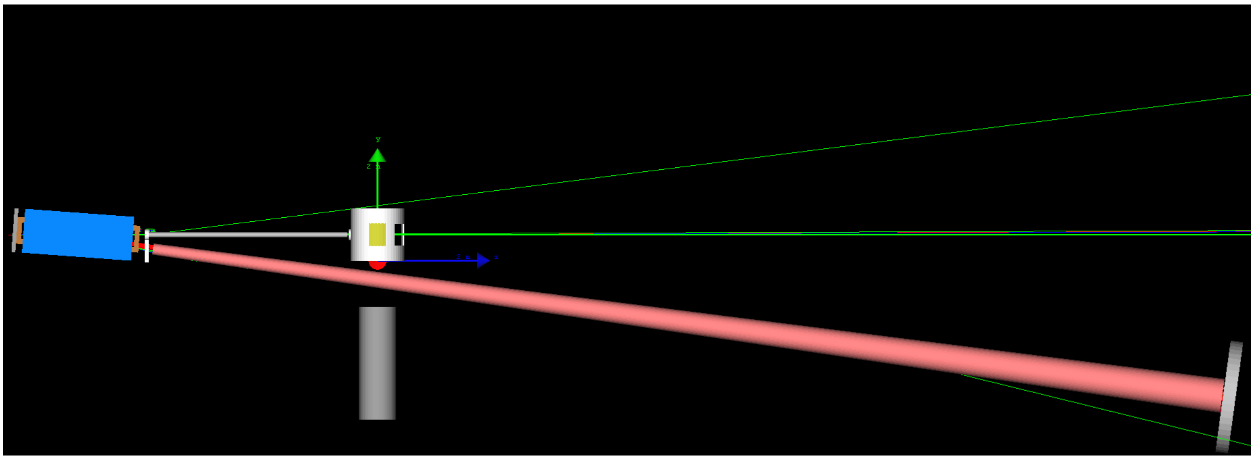

Figure 19: A single dipole deflecting electrons under the target to a beam dump on the floor of the hall. Here 100 events with a 100 MeV cut are shown.

approach that is discussed below. But before we do so we should discuss the differences between a photon and electron beam energy loss in our target as it determines how much current can be put on the radiator (if not restricted by other factors).

A 100 na beam of electrons imposes a heat load of approximately a 1/3 of a Watt on the system. Microwaves contribute up to 1 W and the two sources exhaust the cooling power of our ^{4}He refrigerator. Our simulations agree with power deposit above and they further show that photons per particle, at least in our low Z, thin target, lose about $\frac{1}{5}$ the energy of an electron of the same energy. Further, simulations show that at 1 μA and with a 6% radiator the pure photon beam passing through the target (subject to our spot size requirements) will deposit 0.036 W in the target cell. We have a handwaving argument to support this. With a 10% radiator 10% of the beam energy is converted to photons. We estimate that we lose 50% of the photons in collimator so that only 5% of the beam energy (photons) enters the target. Multiplying this factor by the 0.33 W deposited by a 100 na electron beam and dividing by 5 to account for the effectiveness of a photon to lose energy compared to an electron, we find that a pure photon beam generated by 100 na of electrons on a 10% radiator dumps only 0.0033 W in the target. Scaling this by a factor of 30 here as we plan to put 3μA on the radiator, the power load is a factor of three less than that of a 100 na electrons beam. This argument might be good to 50%.

Careful Geant4 simulations were done to further test this. The test geometry was that of a radiator, the dipole field only (no iron or coils) to deflect the electrons and no collimator. This study found the following: the power deposited in the target cup by the photons produced by a 8.8 GeV, 1 μA electron beam was 0.055 Watts for a 6% radiator and 0.117 Watts for a 10% radiator. Compared with the full model we find that the collimator absorbs about 40% of the photons. What is heartening about this is that it suggests that with 3

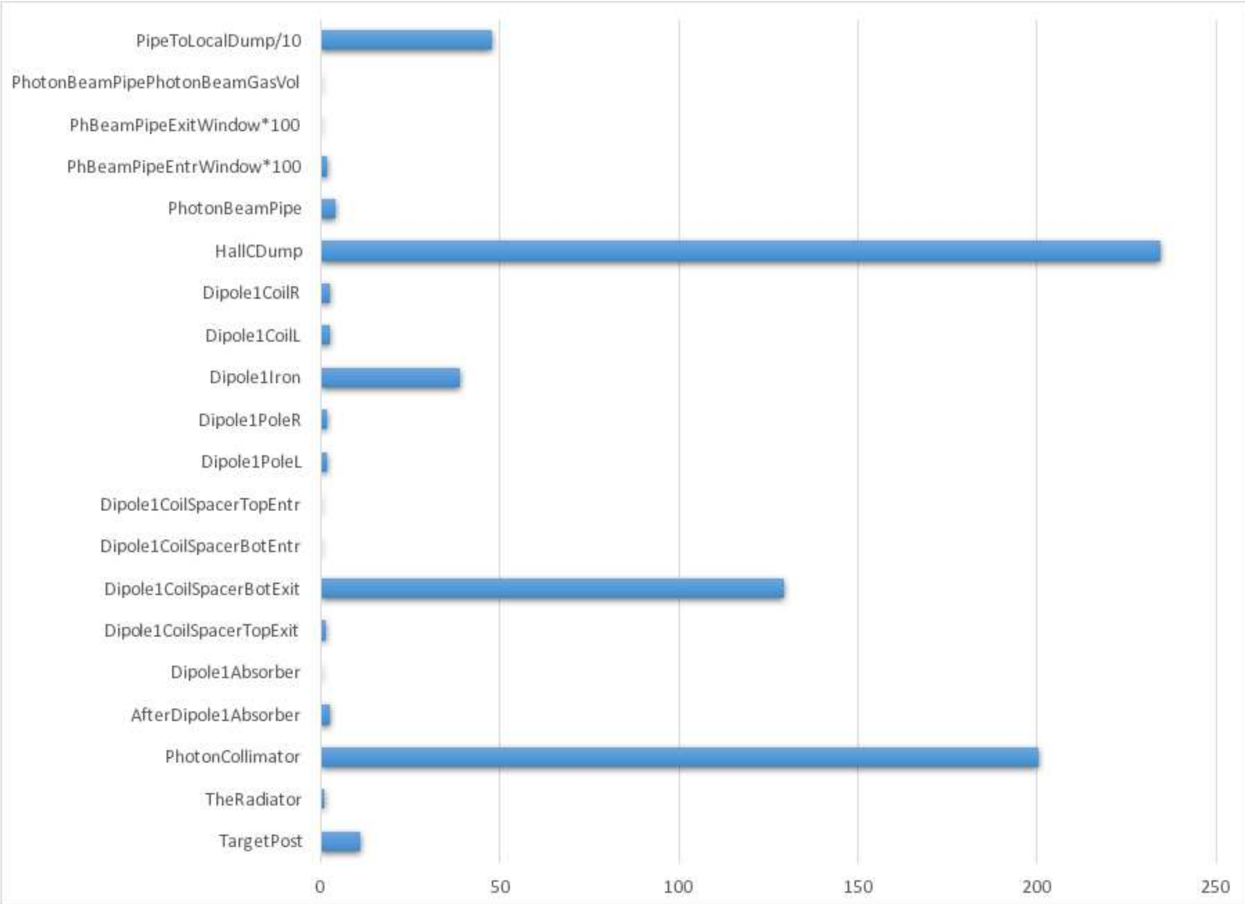

Figure 20: Power lost along beam line with a 8.8 GeV, 1 μA beam and a 6% radiator with beam drifting to a local dump on the floor of the hall. Note that some entries are scaled. We find 86% of the beam power is deposited on the local dump. Power deposited in target is less than 50mW.

or even 5 μA on a radiator we have not approached the cooling power limit of the target refrigerator.

3.3 Uniform illumination of the target cups

Solid polarized targets suffer from radiation damage and local hots spots can also cause depolarization of the target while the imbedded NMR coil samples the polarization over the entire cup. In order to minimize these and to insure accurate NMR readings electron beams have been rastered over the target cup face. This slow raster spirals over the approximate 1 in^2, and when combined with the standard fast raster (2 mm square) insure that the target receives a uniform dose. This is not possible with the photon beam and is also not possible to allow the natural expansion of the photon beam from the radiator to cover the entire cup face. With bremmstrahllung, photons are produced with energies from zero to the end point and elastic events can only be identified by tagging protons in the spectrometer and pointing back to the NPS for the photon responsible. We require knowledge of the interaction location in the target and this is not possible with a diffuse photon beam. The collimator at the end of the first dipole will provide the 2mm resolution needed for reconstruction at the cost of holding the beam location in space fixed. We can still obtain uniform exposure of the target cell by a combined rotation of the target cup synchronized with an up/down movement of the target ladder. See Fig. 23. Rotation of the beam cup is already part of the UVa target group's practices, albeit for different reasons then presented here.

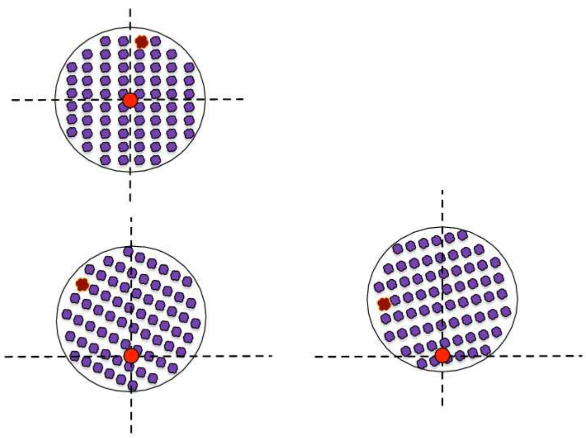

Figure 21: Vertical motion combined with rotation of cup will allow uniform coverage of target cell. The red dot represents the fixed position of the photon beam. The colored bead in the cup can be seen moving as the cup rotates counterclockwise and the target ladder is moved up. Overtime the target receives a full and uniform exposure.

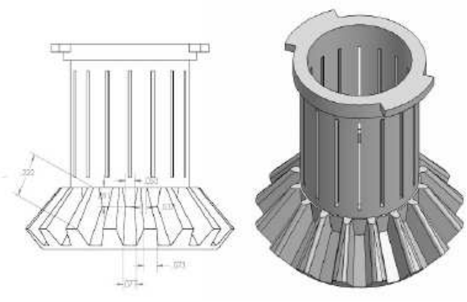

Figure 22: A simple geared cup example used at UVA for rotation.

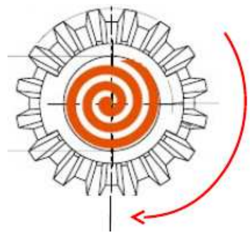

Figure 23: Example of how rotation can move the photon beam spot around the face of the target material.

3.4 The Photon Detector

Participants in this experimental effort are also members of the Neutral Particle Spectrometer (NPS) collaboration who will build the NPS for this and other proposed experiments, for example, E12-13-010, E12-13-007 and unpolarized WACS experiments. The sensitive region of this calorimeter is 30 (horizontal) x 36 (vertical) inches, sitting on a frame allowing for easy movement. The position resolution of the NPS is 3 mm and the energy resolution, $\sigma_E/\sqrt{E}$, is better than 3%.

We plan to place the NPS in three locations. First for $\theta_{cm} = 90°$ at 4.4 GeV the NPS will be at 39° then for 29° for 8.8 GeV. These points are chosen to directly study the s-dependence while holding θ_{γ}^{cm}constant. The NPS is then moved to 47° in the lab frame to acquire the $\theta_{cm} = 120°$ giving a measurement of A_{LL} and A_{LS} at 8.8 GeV that has a direct overlap with the K_{LL} and K_{LS} measurements of Experiment E99-114. This allows a study of the θ_{cm} sensitivity while holding s constant considering the early mention point at $\theta_{cm} = 90°$ at 8.8 Gev. In total we are taking 4 kinematic points the yield the greatest amount of information. These are all critical points from the factorization standpoint due to the large Mandelstam variables where SCET and the handbag model are designed to describe WACS. The spectrometer angle of the HMS, which detects the protons, will be adjusted for each kinematics to match the photon scattering angle. The distance from the target to the calorimeter is chosen to insure an adequate angular coverage of the calorimeter to match HMS.

4 Proposed Measurements

An 80% longitudinally polarized electron beam with current of 3 uA at energies of 4.4 and 8.8 GeV will be used in the proposed experiment. A copper radiator with the thickness of 1.44 mm (10% radiation length) will be installed at 6.2 meters upstream of the target. The circular polarization of the bremsstrahlung photon drops quickly as the photon energy decreases. This relationship is described by Eq. 18:

$$\frac{P_\gamma}{P_e} = \frac{4y - y^2}{4 - 4y + 3y^2}\,, \tag{18}$$

where $y = \frac{E_\gamma}{E_e}$ is the fraction of the photon energy to the electron beam energy. We have optimized the detector acceptance to select those photons that carry 70% to 95% of the incident electron energy. For such bremsstrahlung photons, the average circular polarization is $\approx$ 92% of the polarization of the electrons. The HMS will be used to detect the recoiling proton and the scattered photon will be detected by the future Neutral Particle Spectrometer(NPS).

4.1 The Kinematics

kin. P#	Beam GeV	θ_γ^{cm} deg	θ_{field} deg	θ_γ^{lab} deg	θ_p^{lab} deg	$< E_\gamma^{lab} >$ GeV	P_p GeV/c	L cm	H cm	threshold GeV
P4	4.4	90	0	39	31	3.49	2.40	300	15.9	1.5
P5	8.8	90	0	29	26	6.83	4.00	300	7.2	2.5
P6	8.8	120	-5	47	15.5	6.78	5.80	200	6.8	1.5
P7	8.8	120	275	47	15.5	6.90	5.80	200	17.8	1.5

Table 2: The kinematic parameters of the proposed measurements. θ_{field} is the target field rotation angle, positive means clockwise if looking from the top. $< E_\gamma^{lab} >$ is the average incident photon energy.

Table 2 shows the kinematics parameters of all proposed measurements. We choose to measure A_{LL} at the center of mass angle of 90^o at two s values: one at 4.4 GeV and the other at 8.8 GeV. We also want to measure A_{LL} and A_{LS} at the center of mass angle at 120^o with both a longitudinally and a transversely polarized proton target at 8.8 GeV, providing relatively large t and u values. The geometry of the target magnet coils present some constraints on the available angles. We chose 120^o as E99-114 provides a K_{LL} measurement at this angle. In order to maximize the acceptance for the RCS coincident events, we have to rotate the target field off the axis by 5 degrees. For longitudinal point P6, the target field is rotated clockwise by -5 degrees (looking from the top). For transverse point P7, the target field is rotated clockwise by 275 degrees.

The central momentum of the HMS was determined through a Geant4 simulation and optimized for maximum acceptance of photons with energies from 70% to 95% of the electron beam. In the situation where the momentum acceptance of HMS does not cover the whole range of the considered photon, we will prefer to choose the range of photons with the higher incident energy.

The distance of the front face of the NPS to the target center (L) and its vertical offset (H) are also optimized for maximum RCS event acceptance through the Geant4 simulation. The overlap of the acceptances of the photon arm and proton arms are chosen in a way such that the angular acceptance of proton arm will be fully obtained. Since the target field bends the outgoing proton, those protons detected by HMS have an out-of-plane-angle offset. This generates a compensating out-of-plane-angle offset. Therefore we have to shift the photon arm vertically. These vertical offsets are also listed as H in Table 2. Also listed in the table are the threshold of the photon energy measured by the NPS. This threshold can remove most of the unwanted signal from π^0 events. For details of the kinematic coverage, please refer to Fig. 24, Fig. 25,Fig. 26 and Fig. 27.

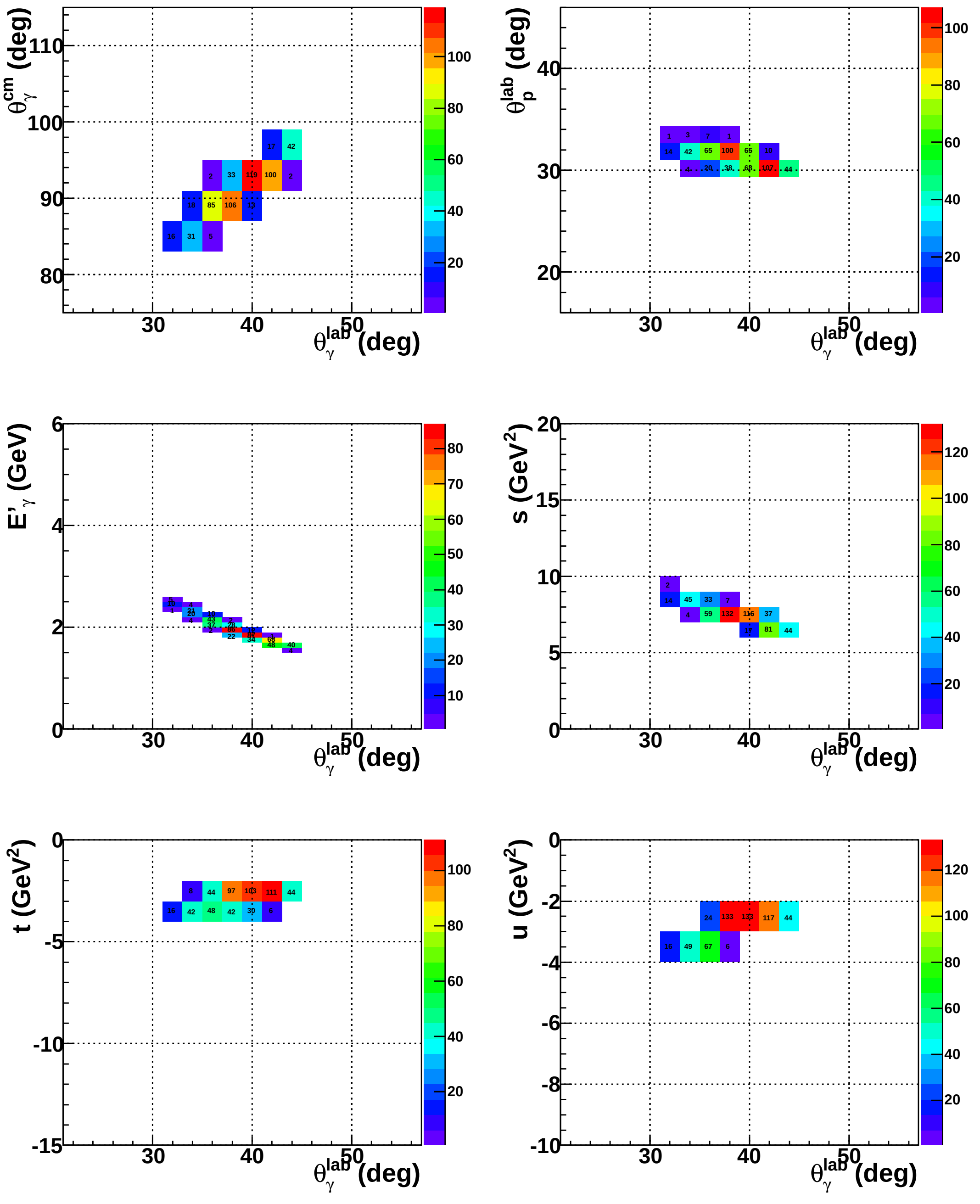

Figure 24: The kinematic coverage for $\theta^{cm} = 60^\circ$ (P4) showing the angular (top) and momentum (middle) distributions for the detected photon (left) and proton (right). The θ_γ^{cm} is the center of mass angle for the photon, θ_γ is the lab angle for the photon, θ_p is the lab angle for the proton, E_γ^f is the photon energy, and P_p is the proton momentum. Also shown in the bottom plots are the Mandelstam variables t (left) and u (right).

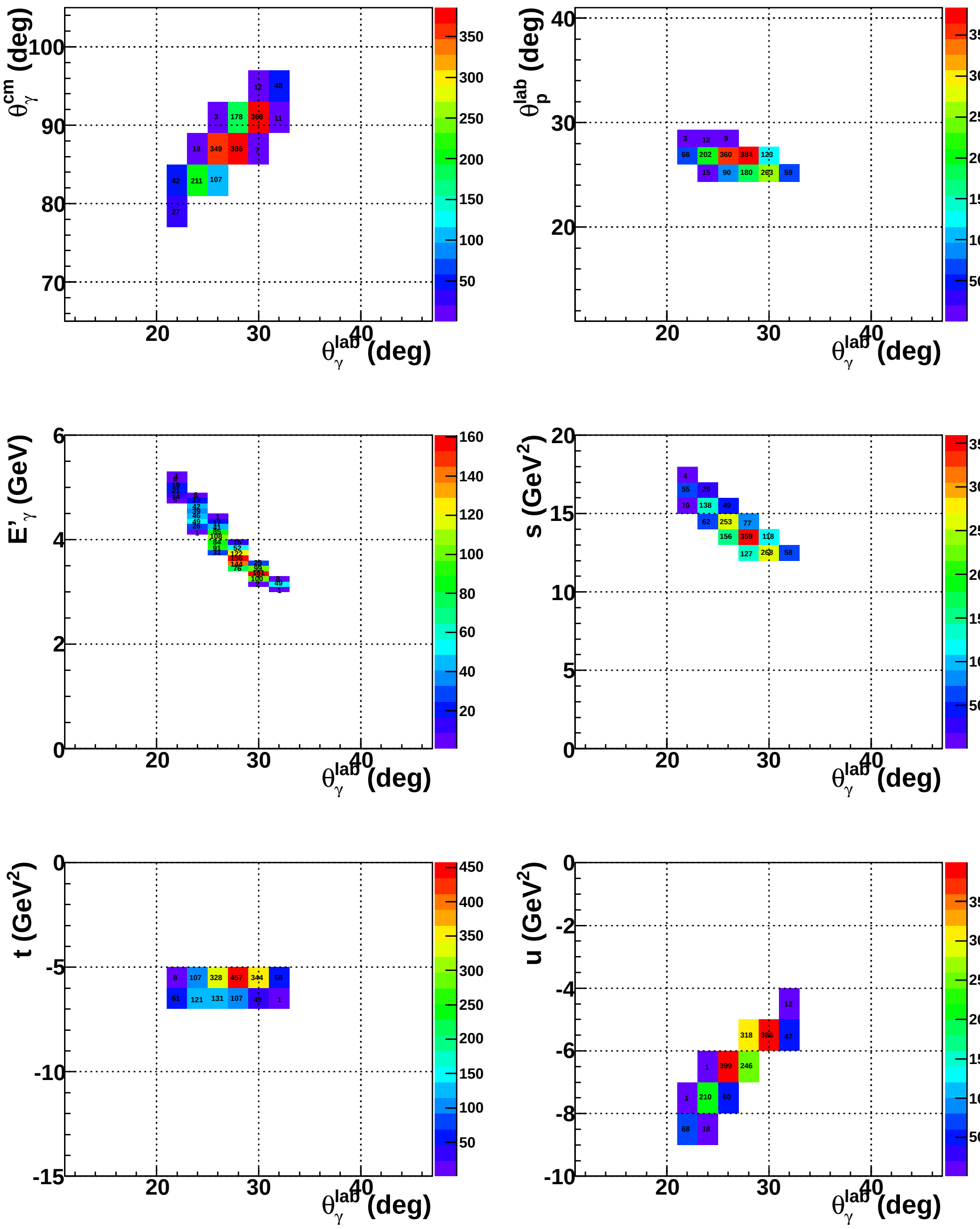

Figure 25: The kinematic coverage for $\theta^{cm} = 90^{\circ}$ (P5) showing the angular (top) and momentum (bottom) distributions for the detected photon (left) and proton (right). The θ_{γ}^{cm} is the center of mass angle for the photon, θ_{γ} is the lab angle for the photon, θ_{p} is the lab angle for the proton, E_{γ}^{f} is the photon energy, and P_{p} is the proton momentum. Also shown in the bottom plots are the Mandelstam variables t (left) and u (right).

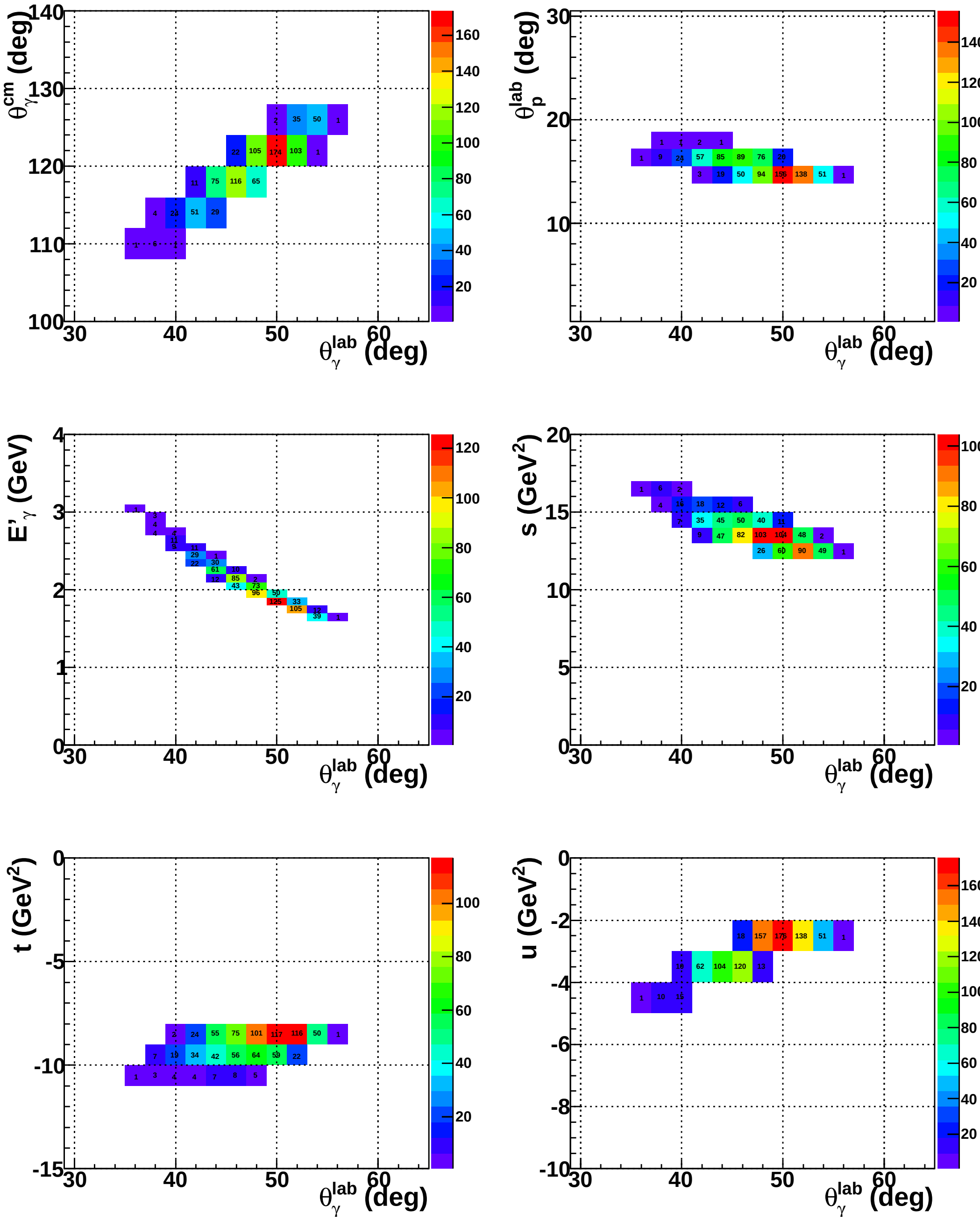

Figure 26: The kinematic coverage for $\theta^{cm} = 136^{\circ}$ (P6) showing the angular (top) and momentum (bottom) distributions for the detected photon (left) and proton (right). The θ_{γ}^{cm} is the center of mass angle for the photon, θ_{γ} is the lab angle for the photon, θ_p is the lab angle for the proton, E_{γ}^{f} is the photon energy, and P_p is the proton momentum. Also shown in the bottom plots are the Mandelstam variables t (left) and u (right).

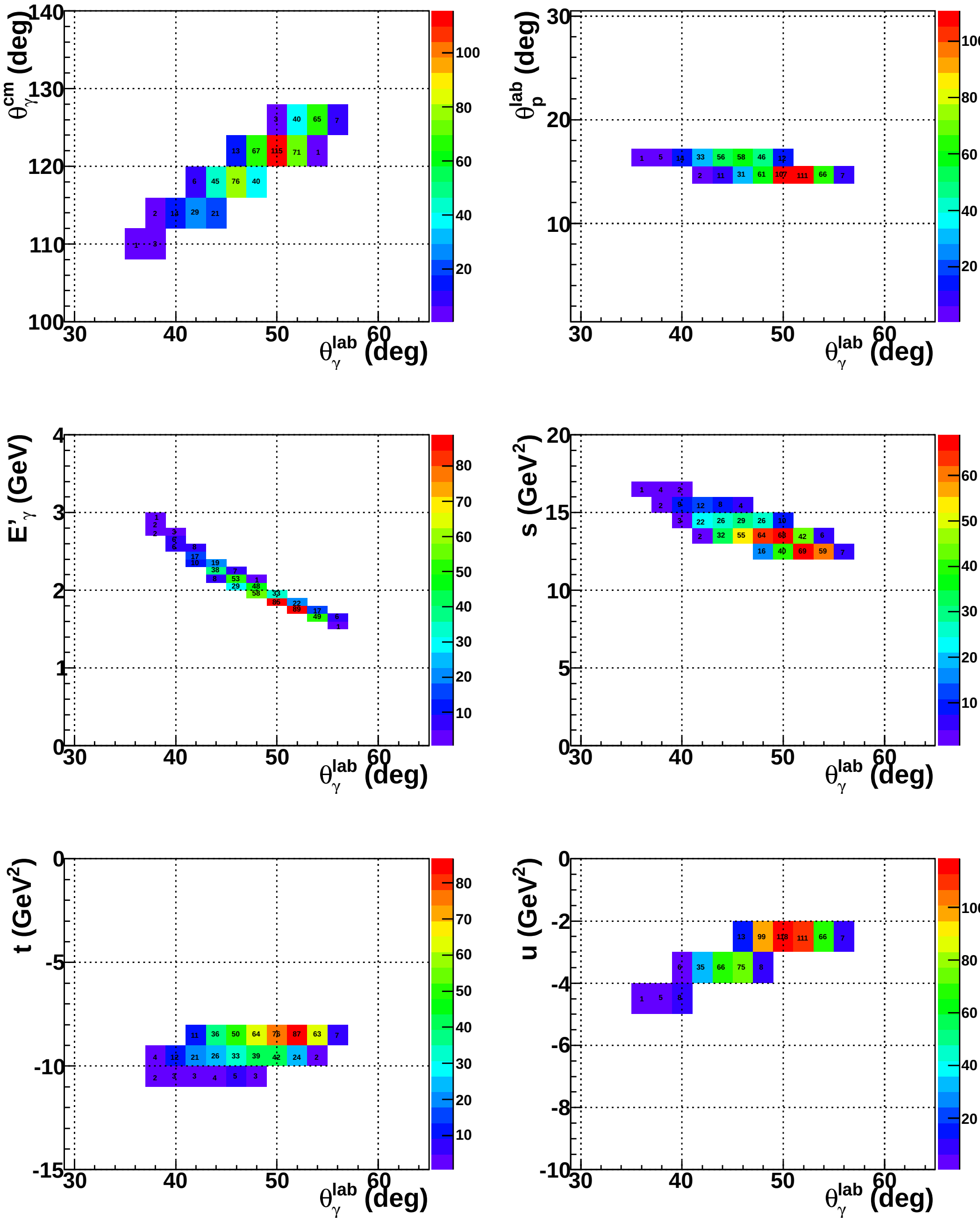

Figure 27: The kinematic coverage for $\theta^{cm} = 136°$ (P7) showing the angular (top) and momentum (bottom) distributions for the detected photon (left) and proton (right). The θ_{γ}^{cm} is the center of mass angle for the photon, θ_{γ} is the lab angle for the photon, θ_p is the lab angle for the proton, E_{γ}^{f} is the photon energy, and P_p is the proton momentum. Also shown in the bottom plots are the Mandelstam variables t (left) and u (right).

4.2 Backgrounds

Comparing to E99-114 or E07-002, these proposed measurements will have much less background since a pure photon source will be used. The primary background comes from neutral pion photo-production from the protons in the target. This background leads to a large dilution factor, which affects the statistical accuracy of the measurements. It can be separated only on a statistical level by using a difference in the shapes of the distribution of RCS and H(γ, π^0) events. We rely on the resolution of the proton arm to predict where to find the Compton photon in the NPS. The Geant4 simulation informs us that both the energy distribution and position distribution of the photon from π^0 decay are much wider than those from real Compton events. Applying RCS correlation cuts (cut on $\delta E/\sqrt{E}$ and δY) using the $\pm 2\ \sigma$ width of real Compton events can significantly reduce the number of π^0 events. $\delta E/\sqrt{E}$ is defined as the difference between measured photon energy in the photon arm and the inferred photon energy (inferred from the measured proton in the proton arm) divided by the square root of the inferred energy. δY is defined as the difference between measured photon horizontal position and the inferred photon horizontal position, in the transport coordinate system and inferred by the detected proton. Fig. 29 shows the RCS correlations cuts from the simulated data. Fig. 30 shows an example of the energy distribution of the H(γ, π^0 p) events; the two vertical lines indicate the 2 σ energy cut location within which the RCS events are extracted. It should be obvious that the energy cut will remove most of the photon which do not carry enough energy. After applying both δE and δY cuts, we can reduce the dilution (D=Total/RCS) to below 10.

The pion can also be produced from bound protons in nitrogen. Motion of the nucleons in nuclei and FSI reduce dramatically the dilution of RCS events. The nuclear pion process was investigated by using E99-114 data obtained from an aluminum target. We found that at conditions similar to those proposed here, pions produced from nuclei increase the dilution factor by less than 10%.

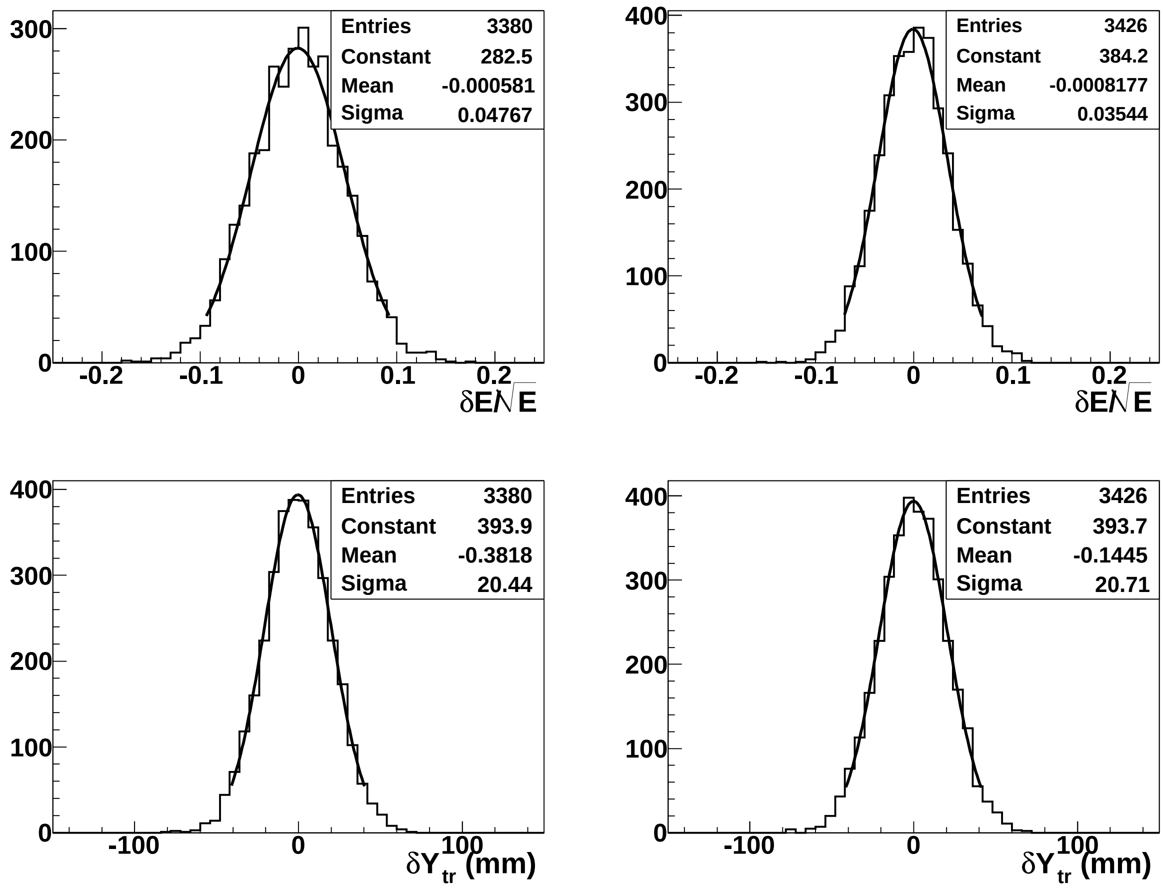

Figure 28: RCS correlation cuts of δE and δY for kinematics P4(left) and P5(right), where δE (top) is the difference between measured photon energy in the photon arm and the inferred photon energy, inferred by the measured proton in the proton arm, and δY(bottom) is the difference between measured photon horizontal position and the inferred photon horizontal position, in the transport frame. A gaussian fit (black curve) is also plotted on top of each histogram, with their fitted parameters labeled in the upper right corner in each panel. A 2σ cut will be used in the data analysis to select good RCS events.

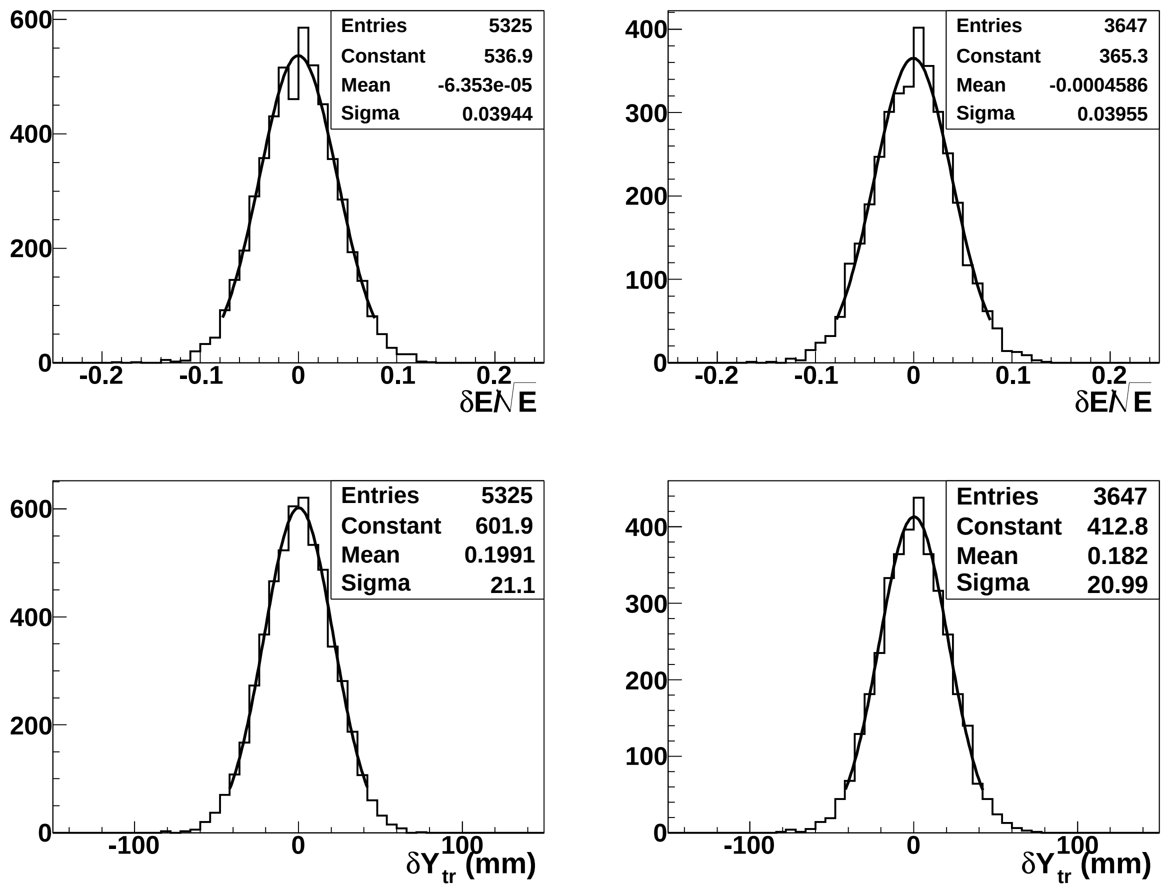

Figure 29: RCS correlation cuts of δE and δY for kinematics P6(left) and P7(right), where δE (top) is the difference between measured photon energy in the photon arm and the inferred photon energy, inferred by the measured proton in the proton arm, and δY(bottom) is the difference between measured photon horizontal position and the inferred photon horizontal position, in the transport frame. A gaussian fit (black curve) is also plotted on top of each histogram, with their fitted parameters labeled in the upper right corner in each panel. A 2σ cut will be used in the data analysis to select good RCS events.

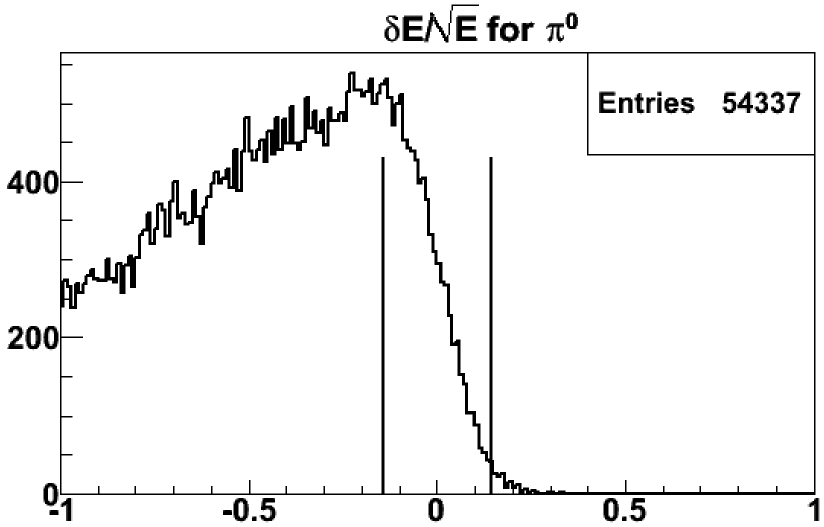

Figure 30: The $\delta E/\sqrt{E}$ distribution for H$(\gamma, \pi^0)X$ events. The two vertical lines indicated the 2σ cut location of extracted RCS events.

4.3 Signal Extraction

It is not trivial to obtain data free of pion events. However, it is possible to obtain data free of RCS events, by selecting different regions of the δX and δY phase space, so that accurate numbers can be obtained for the asymmetry of pion events. It is then possible to measure the asymmetry for pure pion events, the asymmetry for mixed RCS-pion events, and the fraction of the latter events that are RCS. The latter number is just the inverse of the dilution factor D and is obtained by fitting spectra (shown in 35). Each step can contribute to the error in the resulting RCS asymmetry on both a systematic and statistical level. We now consider a technique of directly extracting the real Compton events negating the need for the asymmetry for mixed RCS-pion events.

To reduce uncertainty in the extracted real Compton events it is possible to use a boosted decision tree [47, 48, 49, 50] with multiple discriminating variables. A decision tree is a binary tree structure classifier which organizes the data into regions analyzing event by event. The decision tree algorithm is able to split the phase space into a large number of hypercubes, each of which is identified as either signal or background. The information entropy is used to optimize each split point. The boosting [51] performs best if applied to tree classifiers that, taken individually, have not much classification power. Using a small set of input variables with weak classification power still leads to a great reduction of uncertainty in the extracted counts.

As an example for separation of the RCS events from the pion background we use the discriminating variables δY, δX, and δP. The Monte Carlo is well tuned to the expected resolution of the detection system so that reconstruction of these variables is expected to be within a realistic range in the simulation. The decision tree is then trained and classification using simulated data of signal and the neutral pion background is obtained.

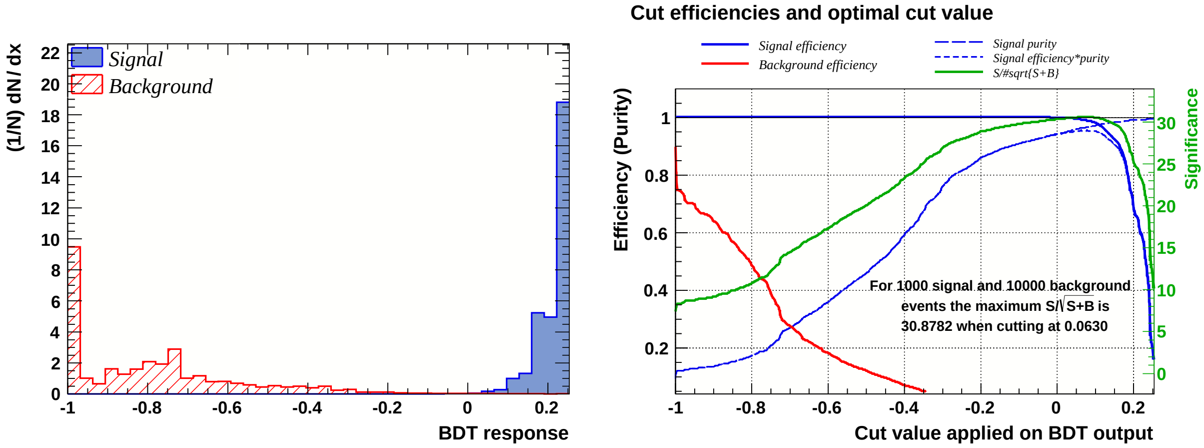

Figure 31: Results of analysis from the training of the boosted decision tree indicating (left) the response of the classifier and (right) the real Compton signal resolving efficiency.

Fig. 31 shows the boosted decision tree output. The result of analysis from the training of the boosted decision tree indicating the response of the classifier is shown in the left plot. The real Compton signal resolving efficiency as a function of the cut on the BDT response is shown in the right plot. Signal efficiency is show in blue and background efficiency is shown in red. The optimal cut is determined by using the derivative of the significance function $S/\sqrt{S+B}$ shown in green. The classifier response indicates that even with the only three mentioned discriminating variable it is possible to obtain greater then 98% signal when making a constraint on the BDT response to eliminate the pion background. The cut value applied on the BDT response is indicated on the right showing that only around 40 events from the pion background survive after the constraint is applied for a situation that started with an order of magnitude more π^0 background than the Compton signal. The separation using a Monte Carlo demonstration is shown in Fig. 32

This technique is especially useful for situations in which the background is difficult to distinguish from the signal in the spectra. Through the use of multivariate discrimination of the phase space even a small signal that is nearly unrecognizable among the background can be separated out with a well defined uncertainty associated with it, given a decent number of discriminating classifiers. For situations like ours with only three classifiers, it is advantageous to expand the feature space by increasing the number of classifiers. Redundant

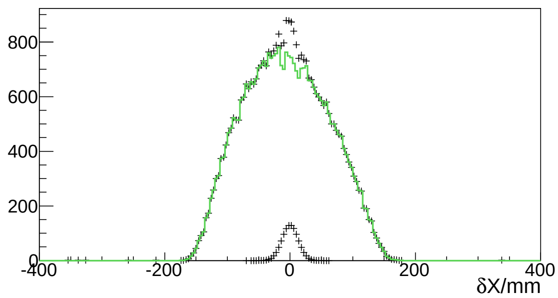

Figure 32: Here we show a δX distribution with signal and background before separation and after. The result of imposing the optimal BDT response cut at 0.063 leading to a RCS event extraction with 98% signal efficiency. This demonstrates a separation with 1000 Compton events with 10000 π^0 background events. This is only a Monte Carlo demonstration. All points that we propose have considerably less background.

variables do no harm, and even with strong correlations between variables all additional information can be used. A good choice in our case would be to use δX, δY, δP, u, s, and t. It the example illustrated the D value was reduced from 11 to 1.04. Clearly there is a statistical advantage to using this type of extraction, but there is all so a systematic advantage. By implementing different cuts in the boosted decision tree response a very thorough study of the asymmetry from the π^0 and RC events can be achieved, allowing very clean distinction between the two. The expect background separation uncertainty can drastically reduced though much of this depends on our ability for the Monte Carlo to match the experimental data in the feature space. We do not rely on these tool in our rates estimation but we expect it to be a very power ally in our analysis.

4.4 Rates and Required Statistics

The event rates are the products of the luminosity, the cross section, and the acceptances of the detectors, as well all other factors such as DAQ dead time and detection efficiency. The rate, N_{RCS} can be calculated as:

$$N_{RCS} = \frac{d\sigma}{dt}_{RCS} \frac{(E^f_\gamma)^2}{\pi} d\Omega_{\gamma p} A_{\gamma p} F_\gamma \mathcal{L}_{e\vec{p}}\,, \tag{19}$$

where $\frac{d\sigma}{dt}_{RCS}$ is the RCS cross section; the factor $\frac{(E^f_\gamma)^2}{\pi}$ is the Jacobian that converts dt to $dEd\Omega$; $d\Omega_{\gamma p}$ is the solid angle of the RCS events that expressed in photon detector; $A_{\gamma p}$ is the acceptance of RCS events in the given range of photon energy E^f_γ; F_γ is the number of photons per incident electron, $\mathcal{L}_{e\vec{p}} = 2.2 \times 10^{36}$ cm^{-2}Hz is the electron-proton polarized luminosity with the NH_3 target, assuming a 60% packing fraction and 3 cm in length. Please note that the 10% radiator is placed 6.2 meters away from the target and we want to collimate the photon spot size on the target to be ± 2 mm in order to achieve good reconstruction for proton. We estimate photon flux lost due to the collimation is 71% for 4.4 GeV and 40% for 8.8 GeV beam energy.

E99-114 measured real compton scattering cross section at four electron beam energy of 2.342, 3.481, 4.620, and 5.759 GeV and θ_γ^{cm} in the range of $60° - 130°$. Table 3 shows their results for the average photon energy of 4.3 GeV. Also shown in the table is the dilution factor D, which is defined as the ratio of total γ seen from the π^0 and Compton signal to the γ seen from the real Compton signal alone: $D = (N_{\gamma,\pi^\circ} + N_{\gamma,\gamma})/N_{\gamma,\gamma}$ for the kinematically correlated photon-proton events.

kin. 4#	θ_γ^{lab}, degree	t, $(\mathrm{GeV}/c)^2$	θ_γ^{cm}, degree	D	$d\sigma/dt$, $\mathrm{pb}/(\mathrm{GeV}/c)^2$
4A	22	-2.03	63.6	2.13	496.
4B	26	-2.57	72.8	1.54	156.
4C	30	-3.09	81.1	1.67	72.
4D	35	-3.68	90.4	2.75	42.
4E	42	-4.39	101.5	2.80	29.
4F	50	-5.04	112.1	2.42	38.
4G	57	-5.48	119.9	2.83	46.
4H	66	-5.93	128.4	3.89	61.

Table 3: The RCS cross section at s = 9 $(\mathrm{GeV}/c)^2$- 4 pass kinematics in E99-114.

To estimate the RCS differential cross section, we adjusted J. Miller's model [46] to match the existing data from E99-114 [52]. Comparing to E99-114 result, Miller's RCS differential cross section model deviates 10% deviation from the 3.1 GeV data, 30% from the 4.3 GeV data and 43% from the 5.3 GeV data. We fit these deviations by a exponential function to get the overall scale factor. Our fitted result is present in Fig. 33.

Miller's model has good constraints on incident photon energy dependence, but not on the dependence of the center of mass angle. We then used a 5th order polynomial function to correct the center of mass angle dependence such that Miller's model matches the E99-114 data. Fig. 34 shows the modified model together with E99-114 data points. For any given photon energy and θ_γ^{cm}, we can use a 2nd order interpolation to calculate the RCS differential cross section. With this modification we are able make estimates for θ_γ^{cm} outside the range of E99-114.

To determine the angular acceptance, we developed a Geant4 simulation program which included the target magnet coils, their magnetic field profile, and the geometry of NPS and

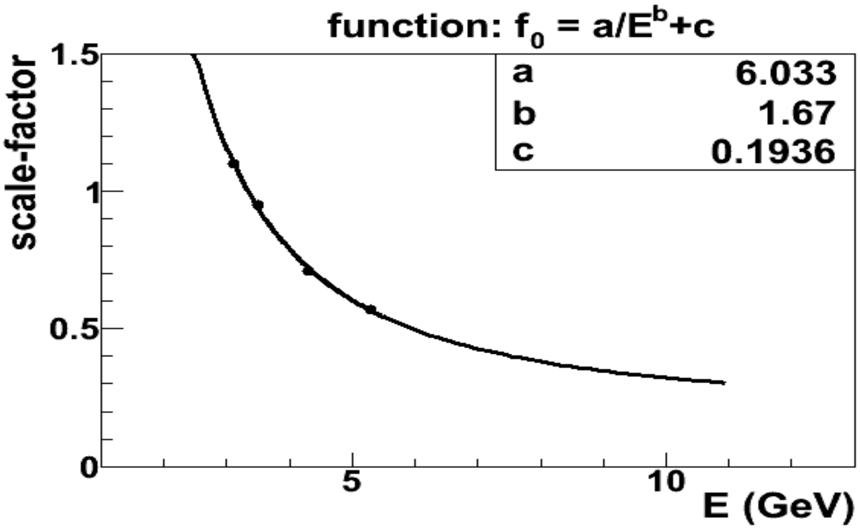

Figure 33: Overall scale factor for Miller's model in order to match E99-114 results [52].

the HMS. We placed the NPS and HMS at optimized locations and simulated RCS events and π^0 backgrounds. Finally we extracted the acceptance for RCS photons in a 3-D space of energy, θ, and ϕ.

The photon flux can be calculated as:

$$F_\gamma = t_{rad}[\frac{4}{3}\ln(\frac{k_{max}}{k_{min}}) - \frac{4(k_{max}-k_{min})}{3E} + \frac{k_{max}^2-k_{min}^2}{2E^2}]\,, \tag{20}$$

where k_{max} and k_{min} are the upper and lower limit of the radiated photon energies, E is the electron beam energy and t_{rad} is the thickness of the radiator in radiation lengths.

Our event rates are integrated over the 3-D space of energy, θ angle, and ϕ angle using Eq. 19. Table 4 shows the rates and dilution factors D. The expected δX distributions for RCS signal and backgrounds after applying the 2σ cuts, are presented in Fig. 35. The pure RCS signal is in red, with a gaussian fit (pink) on top of it. The fitted parameters are labeled in the upper right corner of each panel.

The statistics required for obtaining the specified accuracy of δA_{LL} can be calculated from

$$N_{RCS,required} = D/(P_e P_p f_{e\gamma} \Delta A_{LL})^2$$

where $P_e = 0.80$ is the averaged electron beam polarization, $P_p = 0.75$ is the averaged proton polarization in the target, $f_{e\gamma} = 0.92$ is the ratio of the polarizations to the electron polarizations.

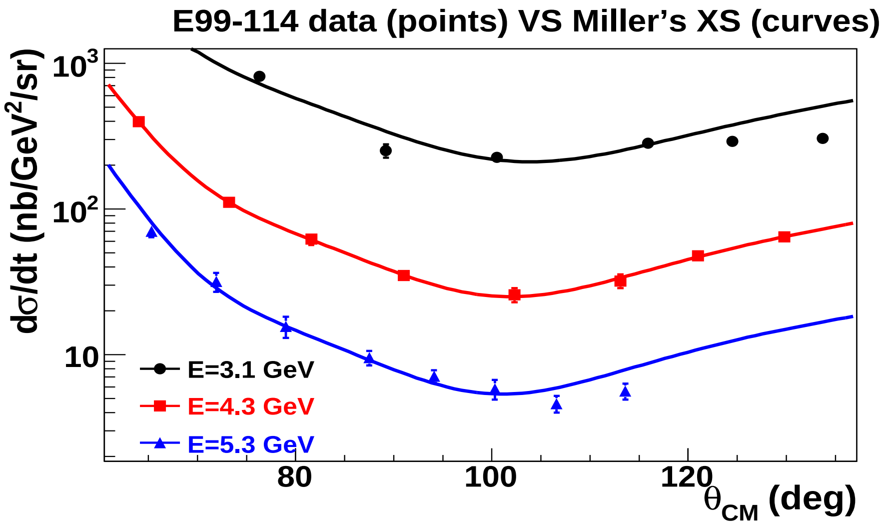

Figure 34: The RCS differential cross section. The solid curve is from modified Miller's model and solid points are from E99-114 [52].

kin. P#	Beam GeV	θ_γ^{cm} deg	θ_{field} deg	time hour	D	stat.	δA_{LL}	s $(\mathrm{GeV}/c)^2$	$-t$ $(\mathrm{GeV}/c)^2$	$-u$ $(\mathrm{GeV}/c)^2$
P4	4.4	90	0	58	3.4	13172	3.0%	7.6	3.0	2.8
P5	8.8	90	0	292	4.5	9814	4.0%	13.6	5.9	6.0
P6	8.8	120	-5	106	4.0	5596	5.0%	13.6	9.0	3.0
P7	8.8	120	275	158	4.1	5724	5.0%	13.6	9.0	3.0

Table 4: The kinematic parameters and the expected counts.

4.5 Systematic Uncertainty

Table 5 shows a list of the scale dependent uncertainties contributing to the systematic error in A_{LL}. With careful uncertainty minimization in polarization, the relative error in the target polarization can be less than 3.9%, as demonstrated in the recent E08-027/E08-007 experiment [53]. Measurements of less than 2.0% have been achieved an ideal test setting at UVA. The electron beam polarization measured by Moller polarimetry will have about 1% uncertainty. The uncertainty in the packing fraction of the ammonia target contributes at a level of 3%.

Charge calibration and detector efficiencies are expected to be known better to 1%. Detector resolution and efficiency is also expect to contribute less than 1%. The signal extraction error will be minimized using a multivariate techniques leading to only a few

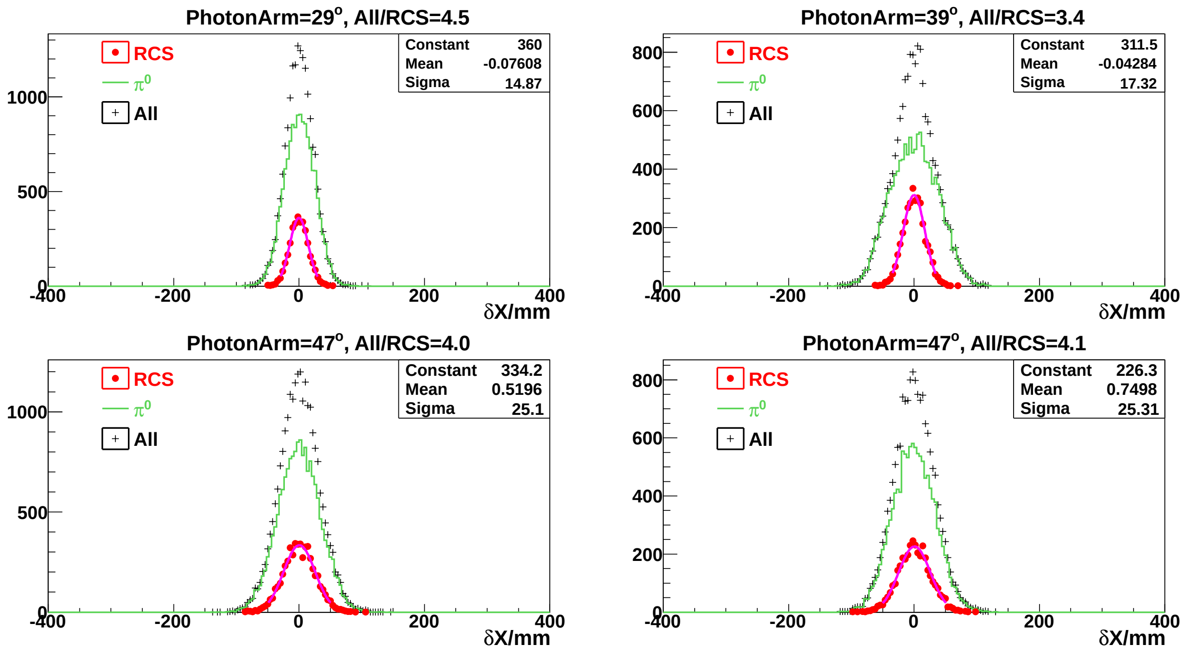

Figure 35: δX distributions after both δE and δY cut, for kinematics P4(top-left), P5(top-right), P6(bottom-left) and P7(bottom-right). The pure RCS signal is red curves, with a gaussian fit (pink) on top of it. The fitted parameters are labeled in the upper right corner of each panel. The π^0 background are ploted as green curve. The total (RCS+π^0) are present as the black points. Also present in the title are the Dilution values.

Source	Systematic
Target Polarimetry	3.0%
Beam Polarimetry	1%
Packing fraction	3%
Trigger/Tracking efficiency	1.0%
Background subtraction	3.0%
Total	$\sim 5\%$

Table 5: Estimation of the systematic errors.

counts of background slipping into the final result. The systematic error on resolving the Compton signal is dependent on the background produced at that kinematic point. A larger background with smaller signal naturally results in a larger error. By considering a larger than expected background we can estimate the expected systematic error from a plausible analysis. We expect less than 3% background which is a estimate directly based on the Monte Carlo.

5 Expected Results and Beam Time Request

5.1 Expected Results

The purpose of this experiment is to measure the initial state helicity correlation asymmetry A_{LL} with a precision sufficient to obtain conclusive evidence on the dominance of the specific reaction mechanism. Another purpose is to determine the form factor ratio: R_A/R_V, which is also related to A_{LL}. We propose to obtain the statistical precision for A_{LL}, given in Table 4 and shown in Fig. 36. Using the handbag formalism to interpret the results of the A_{LL}, we will extract values for R_A/R_V.

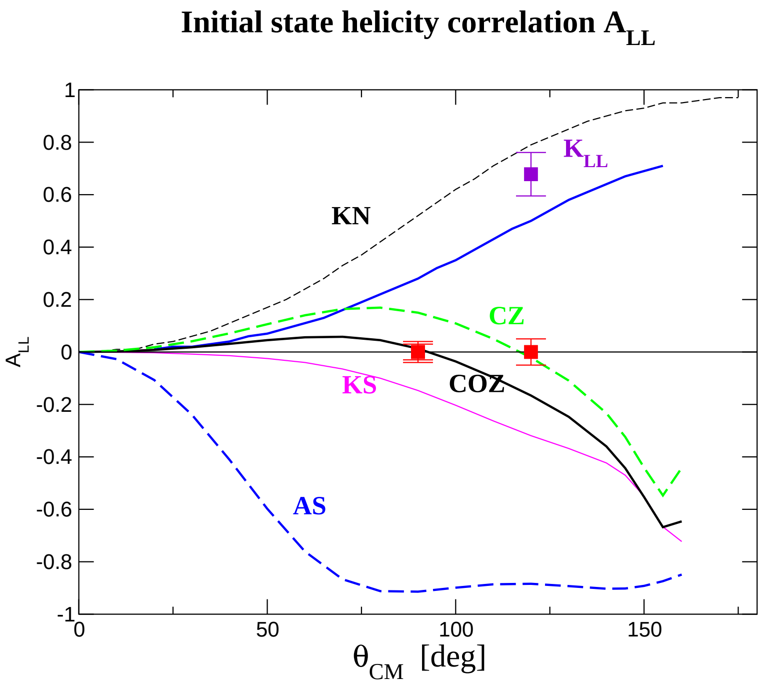

Figure 36: The initial state helicity correlation asymmetry A_{LL} in the RCS process with the expected precision of the proposed measurements shown as closed square. The projected vertical position are arbitrary picked. The labels on the curves are as follows: CQM for the asymmetry in the constituent quark model[25]; the pQCD calculations[3] with AS for the asymptotic distribution amplitudes; with COZ for Chernyak-Ogloblin-Zhitnitsky [45]; GPD for calculations in the soft overlap approach[12]. The K_{LL} result[8] from E99-114 is also shown.

5.2 Beam Time Request

The proposed experiment has one kinematics point using beam energy of 4.4 GeV and three other points using 8.8 GeV, all with currents of 3 uA. In total we request 614 hours for production data taking 4 kinematics points, which are summarized in Table 6.

To measure the packing fraction of the material in the target cell, we need 33 hours in total to do a empty cell and carbon target measurements. We need to measure the beam polarization with the Möller polarimetry every time the beam conditions change. We estimate the frequency to be on the order of once every other day. It will take about 3 hours for each measurement. In total we requested 42 hours.

Kin. P#	Procedure	beam, uA	time hours
P4	production	3	58
P5	production	3	292
P6	production	3	106
P7	production	3	158
	Packing Fraction	3	33
	Moller Measurements	1	42
	Data Beam Time		689
	Target Anneals		54
	Stick Changes		24
	Target commissioning		24
	Kinematics change		12
	BCM,BPM calibration		24
	HMS Optics		8
	Beamline commissioning		24
	Total Requested Time		835

Table 6: The beam time request for the experiment.

It will take about 2 to 3 hours to perform one anneal for the target in order to restore the optimal target polarization. In average we will need an anneal every two days based on the latest experience in E08-007 and E08-027, which ran at 40 nA to 50 nA. In total we estimate there will be 18 times of anneal which results in 54 hours. In the worst case, we might need to remove the target stick 4 times to insert fresh material. Each target material changes will cost about 6 hours. These changes should take about 24 hours in total.

We estimate the kinematics change (move NPS and HMS), from point to point will take about 4 hours each, in total is 12 hours. For each target field angle, we need 24 hours in total (8 hours each) to do optics calibration for HMS optics.

We estimate 8 hours to calibrate the BCMs and BPMs and 24 hours committed to the pure photon beam line.

Combining all the above, the total requested beam time is 835 hours.

6 Technical Considerations

There are already two polarized target experiment approved for Hall C (E12-13-011 and E12-14-006) which will using the same target infrastructure and HMS.

Usually, changing from one experiment to the next would require quite a reconfiguration of the target and detector system. With proper planning the transition from one experiment to the next, the total reconfiguration time would be short since moving the HMS and installing the NPS are all that is required.

The experiment requires support from JLab. In addition to the installation of the polarized target we will also require beam line instrumentation workable at the proposed beam current. The pure photon beam line, in either variant, we require the technical expertise of JLab accelerator, radiation physicist and engineers.

7 The Collaboration

This collaboration consists of members with extensive experience using the UVA polarized target in Hall C. In addition, the collaboration includes many individuals from the RCS collaboration and the NPS collaboration with experience in electromagnetic calorimetry. The JLab target group together with the UVA target group will handle installation, calibration and operation of the polarized target.

8 Summary

We request 835 hours of beam time to measure the initial state helicity correlation asymmetry A_{LL} at θ_γ^{cm}= 90° at two different incident photon energy of 4.4 GeV, s=8 (GeV/c)^2 and 8.8 GeV, s=14 (GeV/c)^2 and $A_{LL}$and A_{LS} at s=15 (GeV/c)^2 at θ_γ^{cm} = 120° overlapping in θ_γ^{cm} with the K_{LL} and K_{LS} measurement in E99-114. This experiment will take place in Hall C, utilizing a 4.4 GeV and 8.8 GeV, 3 μA and 80% polarized electron beam to interact with a radiator and magnets creating a pure photon beam. The UVA/JLAB polarized target (longitudinally and transversely polarized) will be required, as well as the HMS to detect protons, and NPS to detect scattered photons. The proposed configuration provides a unique opportunity to study the initial state target helicity correlations for both longitudinally and transversely polarizations at the idea kinematics significantly adding to the theoretical constraints by increasing the polarized observable portfolio in the WACS phenomenology.

Knowledge of the initial state helicity correlation asymmetry A_{LL} in RCS at these kinematics will allow a rigorous test of the reaction mechanism for exclusive reactions at high t, which is crucial for the understanding of nucleon structure. This experiment will study both the sensitive to s, by measuring two points at different beam energy but the same angle, as well as the sensitivity to θ_γ^{cm} by measuring two points at the same s but different

θ_{γ}^{cm} providing the most information from a single experiment. In addition the overlap of A_{LL} with K_{LL} at $\theta_{\gamma}^{cm} = 120°$ will provide the strictest test of the relationship between these two observables as well as extending the measurement of the proton axial form factor R_A, which is the $1/x$ moment of the polarized parton distribution. The measurement of A_{LS} has a three fold usability. It tests the predictions in the handbag approach, but also tests the relationship between A_{LS} and K_{LS} using the overlapping measurement from E99-114. Finally it can be used in direct extraction of R_T/R_V to an accuracy better than any previous measurement or proposal. Together, the measurement of these observables will help to establish the relationship between F_2/F_1 and R_T/R_V, not only providing a crucial tests of the handbag approach but also helping in improving the parameterizations of the corresponding GPDs $\tilde{H}$ and E.

References

[1] S. J. Brodsky and G. Farrar, *Phys. Rev. Lett.* **31**, 1153 (1973).

[2] V. A. Matveev, R. M. Muradyan, and A. V. Tavkheldize, *Lett. Nuovo Cimento* **7**, 719 (1973).

[3] T. Brooks and L. Dixon, *Phys. Rev.* **D 62** 114021 (2000)

[4] C. Bourrely, J. Soffer, Eur. Phys. J. **C 36** 371 (2004)

[5] M. Jones *et al.*, *Phys. Rev. Lett.* **84**, 1398 (2000).

[6] O. Gayou *et al.*, *Phys. Rev. Lett.* **88**, 092301 (2002).

[7] A. Puckett *et al.*, *Phys. Rev. Lett.* **104**, 242301 (2010).

[8] D. J. Hamilton *et al.* [Jefferson Lab Hall A Collaboration], arXiv:nucl-ex/0410001.

[9] C. Fanelli *et al.*, *Phys. Rev. Lett.* **115**, 152001 (2015).

[10] A.V. Radyushkin, *Phys. Rev.* **D 58**, 114008 (1998).

[11] M. Diehl, T. Feldmann, R. Jakob, P. Kroll, *Eur. Phys. J.* **C 8**, 409 (1999).

[12] H. W. Huang, P. Kroll, T. Morii, *Eur. Phys. J.* **C 23**, 301 (2002), *Erratum ibid.*, **C 31**, 279 (2003).

[13] P. Kroll, private communication.

[14] C. Bourrely, J. Soffer and E. Leader, Phys. Rept. 59, 95 (1980).

[15] F. Cano and J. M. Laget, Phys. Lett.**B 551** (2003); Erratum-ibid.**B 571**:260, (2003).

[16] X. Ji, *Phys. Rev.* **D 55**, 7114 (1997), *Phys. Rev. Lett.* **78**, 610 (1997).

[17] A.V. Radyushkin, *Phys. Lett.* **B 380**, 417 (1996),

[18] N. Kivel and M. Vanderhaeghen, Eur. Phys. J C 75:483 (2015).

[19] N. Kivel and M. Vanderhaeghen, JHEP 1304 (2013) 029; arXiv:1212.0683.

[20] N. Kivel and M. Vanderhaeghen, Nucl. Phys. B883, 224 (2014); arXiv:1504.00991.

[21] N. Kivel and M. Vanderhaeghen, arXiv:1312.5456 [hep-ph].

[22] N. Kivel, private communication.

[23] G. Eichmann and C. S. Fischer, *Phys. Rev.* **D 87**, 036006 (2013).

[24] M. Diehl, P. Kroll, *Eur. Phys. J.* **C 73**, 2397 (2013), arXiv:1302.4604.

[25] G. A. Miller, *Phys. Rev.* **C 69**, 052201(R) (2004).

[26] A. Nathan, R. Gilman and B. Wojtsekhowski, spokespersons, JLab experiment E07-002.

[27] G. P. Lepage and S. J. Brodsky, *Phys. Rev.* **D 22**, 2157 (1980).

[28] A. Radyushkin, arXive:hep-ph/0410276 and Dubna preprint JINR P2 10717.

[29] G. R. Farrar and H. Zhang, *Phys. Rev. Lett.* **65**, 1721 (1990), *Phys. Rev.* **D 42**, 3348 (1990).

[30] A. S. Kronfeld and B. Nizic, *Phys. Rev.* **D 44**, 3445 (1991); M. Vanderhaeghen, P. A. M. Guichon and J. Van de Wiele, *Nucl. Phys.* **A 622**, 144c (1997); T. Brooks and L. Dixon, Phys. Rev. D 62, 114021 (2000).

[31] K. Wijesooriya *et al.*, *Phys. Rev. C***66**, 034614 (2002).

[32] M. Diehl, T. Feldmann, R. Jakob and P. Kroll, *Eur. Phys. J.* **C 39**, 1 (2005) arXiv:hep-ph/0408173.

[33] G. A. Miller, *Phys. Rev.* **C 66**, 032201 (2002).

[34] M. Diehl, T. Feldmann, H. W. Huang and P. Kroll, Phys. Rev. D **67**, 037502 (2003) [arXiv:hep-ph/0212138].

[35] E. Lomon, *Phys. Rev.* **C 66**, 045501 (2002).

[36] R. L. Anderson *et al.*, *Phys. Rev.* **D 14**, 679 (1976).

[37] M. Battaglieri *et al.*, *Phys. Rev. Lett.* **87**, 172002 (2001).

[38] T. H. Bauer *et al.*, Rev. Mod. Phys. **50**, 261 (1978).

[39] M. A. Shupe *et al.*, *Phys. Rev.* **D 19**, 1921 (1979).

[40] C. Perdrisat *et al.*, JLab experiment E01-109, 2001.

[41] N. Dombey, Rev. Mod. Phys. 41, 236 (1969).

[42] N. Dombey, Rev. Mod. Phys. 41, 236 (1969).

[43] T. W. Donnelly and A. S. Raskin, Ann. Phys. (New York) 169, 247 (1986); 191, 81 (1989).

[44] Spin Asymmetries of the Nucleon Experiment, JLAB E-03-109, O.Rondon, Z.E. Meziani, and S. Choi, spokespersons.

[45] V. L. Chernyak A. A. Oglobin, and A. R. Zhitnitsky, *Z. Phys.* **C 42**, 569 (1989).

[46] G. Miller, Phys. Rev. C, 69, 052201.

[47] L. Breiman, J. Friedman, R. Olshen and C. Stone, “Classication and Regression Trees”, Wadsworth International Group, Belmont, California (1984).

[48] J. Friedman, T. Hastie, and R. Tibshirani, “Additive logistic regression: a statistical view of boosting”, Annals of Statistics 28 (2), 337-407 (2000).

[49] Y. Freund and R.E. Schapire, A short introduction to boosting, Journal of Japanese Society for Artificial Intelligence, 14(5), 771-780.

[50] J. Friedman, Recent Advances in Predictive (Machine) Learning, Proceedings of Phystat2003, Stanford University, (September 2003).

[51] R.E. Schapire, The boosting approach to machine learning: An overview, MSRI Workshop on Nonlinear Estimation and Classification, (2002).

[52] A. Danagoulian *et al.*, Phys. Rev. Lett, 98, 152001 (2007).

[53] D. Keller, Nucl. Inst. and Meth. A 728 133-144 (2013)

[54] C.D. Roberts, M.S. Bhagwat, A. Holl, and S.V. Wright, Eur. Phys. J. Spec. Top. 140, 53 (2007)

[55] I.C. Cloet, G. Eichmann, B. El-Bennich, T. Klahn, and C.D. Roberts, Few-Body Syst. 46, 1 (2009)